Journal of
Materials Chemistry A

ROYAL SOCIETY
OF CHEMISTRY

REVIEW

View Article Online
View Journal | View Issue

Cite this: *J. Mater. Chem. A*, 2025, **13**, 1590

Unlocking recent progress in niobium and vanadium carbide-based MXenes for sodium-ion batteries

K. Karuppasamy, †[ab] Ganesh Kumar Veerasubramani, †[ac] Vishwanath Hiremath,†[d] Dhanasekaran Vikraman, †[e] P. Santhoshkumar,[f] Georgios N. Karanikolos, [gh] Ali Abdulkareem Alhammadi,*[ac] Hyun-Seok Kim [e] and Akram Alfantazi*[ab]

The performance of electrochemical energy storage (EES) devices is determined by the inherent characteristics of electrode materials such as anodes and cathodes. 2D materials are increasingly being studied for their unique structural and electrochemical properties. Various materials, including transition metal oxides, metal sulfides, phosphides, and metal–organic framework (MOF) compounds, have been explored as potential anodes for sodium storage. However, challenges include significant volume and conductivity changes, cyclability, low capacity, and hindered overall rate performance in sodium-ion batteries (SIBs). Employing 2D-layered transition metal carbides and nitrides (MXenes) and their functionalized/surface-modified composites provides a promising strategy for minimizing volume expansion during charge–discharge, enhancing mass transport, and improving conductivity, thereby improving the specific capacity, rate capability, and cycling stability of SIBs. This review examines the ability of two specific MXene compounds, namely niobium carbide (Nb–C) and vanadium carbide (VC), to be advanced electrode materials for enhancing the performance of SIBs. Furthermore, it comprehensively analyses recent developments in SIB anodes based on Nb–C and VC hybrid materials, shedding light on their electrochemical and structural properties. Last, the crucial challenges of Nb–C and VC electrodes employed in SIBs are explained, and future prospects for the SIB application of these electrodes are elaborated.

Received 13th August 2024
Accepted 6th November 2024

DOI: 10.1039/d4ta05669h

rsc.li/materials-a

1. Introduction

In day-to-day life, global warming, high fuel prices, pollution, and geopolitical concerns affect society's dependency on fossil fuels and have profound implications for the future.[1–4] Promoting advanced electrochemical energy storage (EES) technologies and energy resources is essential to minimizing these concerns.[2,5–9] In recent years, a rapid rise in the demand for large-scale systems that store energy has been seen, with significant capacities, at low prices, and with superior energy density.[1] Over the past two decades, lithium-ion batteries (LIBs) have presented various fascinating pathways, as well as challenges, in EES systems, being essential for portable electronics, electric vehicles, and space satellites.[2,10,11] As a result of the development of their manufacturing processes and the increasing global energy demand, LIBs have seen an increase in demand. Also, the rapid consumption of precious lithium and transition metals cobalt and nickel (Co and Ni) will increase their prices.[12,13] Next-generation energy EES systems are critically important for portable and stationary electronics exhibiting high energy density, long life cycle, and reasonable cost.[9,14] A wide range of novel energy storage systems have been proposed as affordable energy storage solutions, including lithium/sodium-air batteries, sodium/potassium/zinc-ion batteries, lithium/sodium-sulfur batteries, and magnesium/sulfur batteries.[9,15–17] SIBs are among the most popular candidates for performance-driven EES devices due to their earth abundance and high energy density.[18] There has also been

---

[a] *Department of Chemical and Petroleum Engineering, Khalifa University of Science and Technology, Abu Dhabi, 127788, United Arab Emirates. E-mail: ali.aalhammadi@ku.ac.ae; akram.alfantazi@ku.ac.ae*

[b] *Emirates Technology Center, Khalifa University of Science and Technology, Abu Dhabi, 127788, United Arab Emirates*

[c] *Center for Catalysis and Separation (CeCaS), Khalifa University of Science and Technology, Abu Dhabi, 127788, United Arab Emirates*

[d] *Department of Chemistry, Kishkinda University, BITM Campus, Ballari 583104, Karnataka, India*

[e] *Division of Electronics and Electrical Engineering, Dongguk University-Seoul, Seoul 04620, Republic of Korea*

[f] *Department of Mechanical and Nuclear Engineering, Khalifa University of Science and Technology, Abu Dhabi, 127788, United Arab Emirates*

[g] *Department of Chemical Engineering, University of Patras, 26504, Patras, Greece*

[h] *Institute of Chemical Engineering Sciences, Foundation of Research and Technology-Hellas (FORTH/ICE-HT), 26504 Patras, Greece*

† These authors contributed equally.

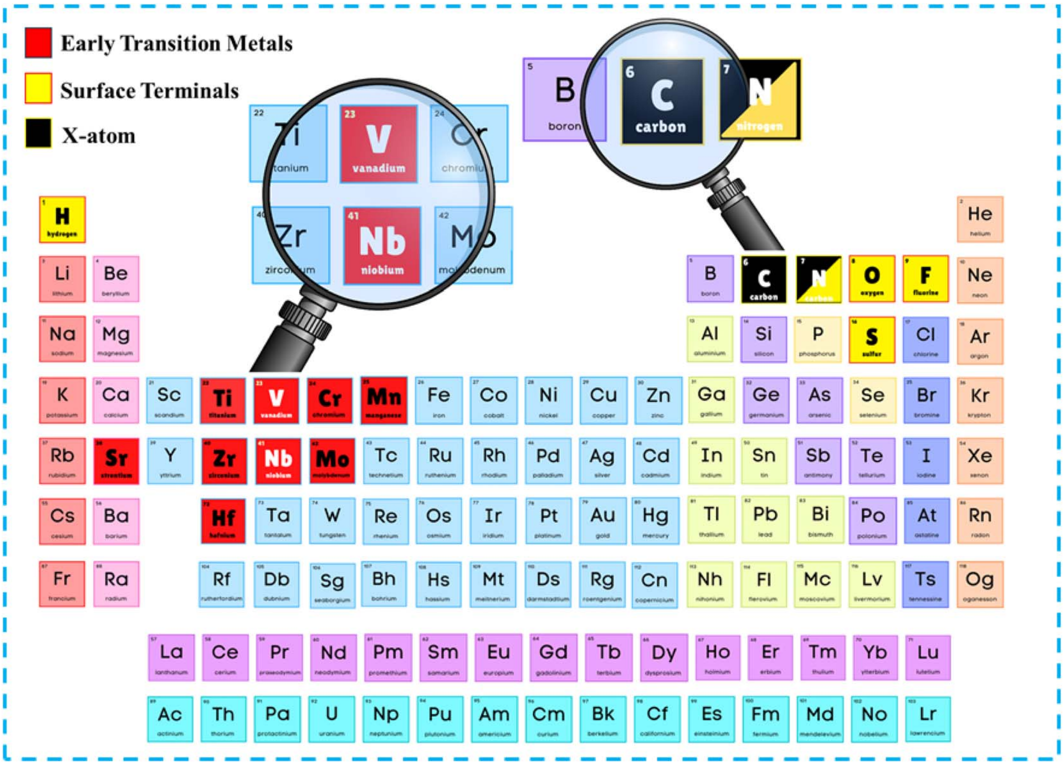

Fig. 1 The periodic table illustrates the early transition metals, surface terminals, and X-atoms found in various MXenes used for SIBs, with each group marked in distinct colors.

tremendous interest in SIBs combining high energy density with low material costs.[19]

Due to the abundance of sodium, SIBs have become promising energy storage technologies in recent years. However, certain anode materials face constraints due to the slight disparity in their ionic radii, with sodium measuring 1.02 Å.[19] Graphite is a widely investigated anode material for LIBs; however, it has an unsatisfactory specific capacity of 35 mA h g^{-1} when employed in SIBs.[20] High-capacity anode materials are necessary to achieve fast charge/discharge mechanisms in SIBs.[21] Because of their promising mechanical, electrical, and optical features, two-dimensional electrode materials are gaining high interest in flexible nanoelectronics, solar cells, sensors, and EES devices.[21] Furthermore, most two-dimensional (2D) materials are scalable, making them suitable for mass production. 2D materials such as metal oxides, carbides, nitrides, hexagonal boron nitride (h-BN), 2D-layered transition metal carbides/nitrides (MXenes), 2D transition metal sulfides, and phosphides have rapidly developed in the past few decades.[17,22–24] Despite this, developing 2D electrodes for SIBs still faces difficulties, including synthesis, elaboration of growth mechanisms, and an unknown mechanism of electrochemical processes.[25] These layered transition metal carbide and nitride phases of MXenes comprise the MAX phase's layering form ($M_{n+1}AX_n$), where the value of "n" can be either 1, 2, or 3, "M" stands for a d-block transition metal element (Ti, Zr, Ta, Mo, Ta, Nb, V, Zr, *etc.*), "A" for 13 and 14 groups of elements, and "X" for nitrogen and carbon.[25]

MXenes have hydrophilic surfaces due to their terminated groups, such as fluorine, oxygen, and hydroxyl.[16,26,27] They can be used to make thin films, devices, and coatings, since they are easy to process and require lower activation energy, thereby leading to plausible applications in water splitting, triboelectric nanogenerators, batteries, and supercapacitors.[28] Due to the fast diffusion of lithium and sodium ions on their surfaces, MXenes can also have high rates and storage capacities.[16,26,27] However, some of these 2D materials face challenges, including the reaction between discharge products and electrolytes, which can be resolved by isolating the electrolytes and electrodes. As a result of alloying and conversion reactions, some 2D materials are limited in their reversibility after discharge, resulting in poor rate performance.[20,29] This problem could be resolved by optimizing the composition of electrolytes and the design of nanostructures. Chemical reactions and large-volume changes can be triggered by the significant accumulation of sodium (Na^+) ions, which results in poor initial capacity retention and poor coulombic efficiency.[1,2] Introducing a protective layer onto the product's surface would be a promising solution to sort out those problems. When considering all factors, finding anodes with large specific capacities, low redox voltage plateaus, and especially high-rate capabilities is crucial.[1,2]

In contrast to traditional titanium and molybdenum-based MXenes, V and Nb-based MXenes are plentiful in the Earth's crust, lowering the capital expenditure associated with producing the suggested electrode materials.[30–32] Moreover, they exhibit beneficial characteristics such as enhanced power performance, extended cycle life, and elevated energy and power densities.[32] Furthermore, the robust carbide bonds in Nb–C and VC carbides enable the accommodation of more sodium ions, improving coulombic efficiency and reversible capacity.[33] VC possesses a superior theoretical capacity (~300 mA h g^{-1}) and provides exceptional electrical conductivity, rendering it appropriate for applications necessitating high energy density and power performance.[34] Conversely, Nb–C offers superior structural stability during volumetric fluctuations and improves cycling and long-term performance by generating a more stable solid electrolyte interphase (SEI). VC may be more suitable for high-capacity and rapid charging applications, while Nb–C may be more ideal for applications requiring consistent performance over prolonged cycles.[35,36] Few recent studies have summarized the latest progress of MXenes as advanced anode electrode materials for SIBs.[22,37–39]

Very recently, Cao and coworkers have comprehensively reviewed the importance of MXenes and their composites as potential electrodes for SIBs, highlighting the complete preparation, physicochemical properties, and electrochemical performances of various MXenes.[39] The current review provides a more focused and in-depth analysis of the physicochemical and electrochemical performance of vanadium carbide (VC) and niobium carbide (Nb–C) MXenes in SIBs. Although research on these materials as electrode components for SIBs is still in its early phases, they provide significant advantages such as excellent conductivity, stability, and the potential to be modified with surface groups, which can improve their electrochemical performance. Considering the wide availability of sodium sources and the significant economic consequences of SIBs, materials such as VC and Nb–C have the potential to contribute significantly to the widespread use of large-scale SIB applications.[36] Fig. 1 highlights the theme of the present review in the periodic table with early transition metals, surface terminals, and X-atoms found in various MXenes utilized for SIBs, with each group marked in distinct colors. This targeted approach highlights their potential in advancing SIB technology, especially concerning their unique electrochemical properties, such as high specific capacity, superior rate performance, and extended cycle life. Further, it differs from the reported literature because it comprehensively evaluates the new progress and improvements in VC and Nb–C MXenes, along with their surface modification tactics by incorporating carbon and functionalization through metal sulfides. In addition, a specific focus on these VC and Nb–C materials and their unique capacity to boost coulombic efficiency has been elaborated. This review unlocks their potential and fully expedites their commercial feasibility.

2. Background of MXenes

A timeline diagram in Fig. 2 highlights the development of various MXenes for diverse EES applications.[40–49] It highlights the chronological progression and specific advancements of MXene materials in fields like LIBs, supercapacitors, non-lithium-ion batteries, air batteries, and sulfur/selenium batteries after MXenes were discovered in 2011.[42,50]

Since the discovery of MXenes by Gogotsi *et al.* in 2011, researchers have shown massive interest in MXenes, and they have emerged as a significant class of layered 2D materials among the many different types of 2D materials.[42,50] More than 30 different MXenes have been successfully synthesized experimentally, and over 100 theoretical MXenes with various physical and chemical properties have been anticipated.[51,52] Among the various studied MXenes, $Ti_3C_2T_x$ is one of the most extensively studied materials, which can be produced by selective monoatomic Al layer etching inside the Ti_3AlC_2 MAX phase precursor using hydrofluoric (HF) acid as the potential etchant.[52] Due to their layered structure and exceptional performance, MXenes show promise in several sectors (Fig. 3), including electrocatalysis, electronics, EMI shielding, energy storage, sensing, biomedical, *etc.*[53,54]

2.1. Structure and properties of MXenes

The MXene fabrication processes, structure, and properties are extensively covered in the literature.[28,55–60] Henceforth, this section provides a few salient features of reported MXenes. There are two main ways to synthesize MXenes: top–down and bottom–up approaches.[33,52] In the top–down approach, the MXenes are produced by separating the MX phase from their

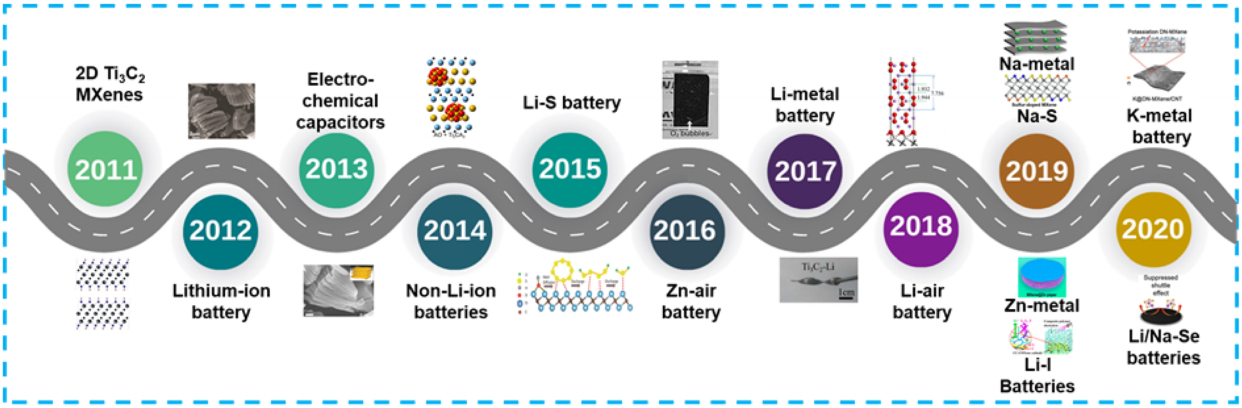

Fig. 2 Schematic timeline diagram illustrating the development of various MXenes for diverse energy storage applications.

Fig. 3 Advantages and various applications of MXenes in different sectors.

bulk MAX counterparts. In the case of bottom–up approaches, the MXenes are obtained from molecules or atoms, for example, α-Mo_2C, resulting in MXenes with more excellent transverse dimensions and fewer defects, which helps research their intrinsic features.[61] Plenty of the reported MXenes have been prepared through a top–down process that exhibits the selective etching of atomic layers (such as Al, Ga, and Si) from the MAX phases.[50,53,54] Solid solutions and organized double-transition metal structures are among the several ternary carbides and nitrides that make up the MAX phase. The hexagonal structure could be obtained by sandwiching element A between transition metal carbide or nitride layers. Since the M–A bonds are metallic, isolating the $M_{n+1}X_n$ layers and forming MXenes by mechanical shearing of the MAX phase is impossible.[54] Furthermore, selective etching of the A-element layers is made possible by the better chemical activity of M–A bonds than M–X bonds. Henceforth, choosing an appropriate etchant is crucial for a productive bottom–up process.

Earlier, Gogotsi and the team used one of the popular etchants, the HF etchant, to convert Ti_3AlC_2 to $Ti_3C_2T_x$.[33] After HF treatment, an accordion-like structure was formed by converting the dense Ti_3AlC_2 solid to a multilayered loosely packed $Ti_3C_2T_x$ structure. The other alternative, a strong acid and fluoride salt mixture, such as HCl and LiF, was also employed to prepare the MX phase.[62] The LiF-HCl etchant produced less critical but more considerable lateral flaking $Ti_3C_2T_x$ with larger layer spacing than HF. Intercalation of water or cations (Li^+) likely reduced the interlayer connections, leading to this result. Etching techniques that use acid-fluoride salt combinations (*e.g.*, NaF, KF, and NH_4F) have also been successfully developed.[63] In addition, MXenes can be synthesized using various techniques, including molten salt etching and alkali etching.[64,65] After HF etching, the multilayer MXenes can be intercalated to create less or monolayer MXenes. Isopropylamine and other polar chemicals can intercalate with these few-layer MXenes, as can larger organic base molecules. Following intercalation, few-layer MXenes can be treated in water using sonication or mechanical vibration to create colloidal solutions. However, an additional intercalation step is unnecessary when etching with acids and fluoride salts (such as HCl and LiF). MXenes will already have embedded metal cations once they are etched. One way to introduce these cations is by gently mechanically vibrating the solution, such as shaking it.[65]

MXenes have $P6_3/mmc$ space group symmetry like MAX phases and a hexagonal compact packing (hcp) crystal structure.[66] Various formulations of MXenes are available, each with its unique structure. Some examples are M_2X, M_3X_2, and M_4X_3.[66] Wet chemical etching typically results in the complete termination of MXenes, introducing surface atoms including O, F, OH, H, and Cl. DFT calculations have confirmed that functionalized MXenes are thermodynamically stable. A notable difference between completely functionalized and partially functionalized MXene surfaces is the former's stability. The layered structure of MXenes improves functional groups on numerous surfaces.[62,67] Chemical groups on the surface of MXenes are distinctive, depending on the exact composition and balance of the elements. The exceptional chemical properties of MXenes make them stand out in the 2D material space. Their hydrophilic terminal groups, which can be O or OH, and these terminal functional groups are the reason for their exceptional metal conductivity.[67] The various advantageous properties of MXenes are pictorially represented in Fig. 3. Some of the salient points are briefed herein.

(a) Electronic properties: MXenes' strong conductivity is one of their essential characteristics. MXenes are very conductive to heat and electrons because of their metallic characteristics. These characteristics result from their layered structure, in which functional groups (such as hydroxyl, fluorine, or other elements) or other components separate the transition metal carbides and nitrides.[68,69] MXenes' electrical characteristics can be adjusted by altering the surface functional groups and intercalating distinct species between the layers. Their tunability, which is essential for various applications, allows them to adjust their electrical conductivity.

(b) Optical properties: MXenes have powerful light–matter interactions and tunable plasmonic features, among other interesting optical properties.[69] Applications in photocatalysis, sensing, and optoelectronics are drawn to these qualities. Certain MXenes can absorb light, particularly in the visible to near-infrared spectrum.[70] MXenes can produce electron–hole pairs in light, enhancing the number of charge carriers at the surface. Extensive research has been conducted on MXenes as an active photodetector component.[70]

(c) Electrochemical properties: the quick storage and release of charge are made possible by MXenes' high specific capacitance. Additionally, ion intercalation and deintercalation reactions using MXene materials are reversible.[71] Furthermore, they are involved in faradaic reactions, in which redox processes take place at the electrode–electrolyte interface to facilitate charge transfer.[61] Additionally, MXenes have a high dielectric constant. Because of all these qualities, MXenes can be utilized as an active component in supercapacitors and batteries.[72,73] Because of their layered structure and nanoscale interlayer spacing, MXene materials offer effective channels for ion diffusion. Quick ion diffusion promotes fast charge and discharge rates in batteries and supercapacitors, making fast energy storage and retrieval possible.

(d) Magnetic properties: it is essential to observe that not all MXenes exhibit intrinsic magnetic properties, which largely depend on the choice of others that can exhibit antiferromagnetic, ferromagnetic, or paramagnetic behavior.[70,73] The magnetic properties of MXenes can be tuned by altering the chemical composition and controlling the surface terminations.

3. Niobium (Nb) carbide-based anodes for SIBs

3.1. Synthesis of niobium carbide-based MXenes

Over fifty years have passed since the discovery of niobium-carbon systems, which contain five solid single-phase regions: a solid carbon solution in niobium (bcc), Nb_2C (hcp), Nb–C (fcc), z-Nb_4C_{3-x}, and z-NbC_{1-x}.[3,4,74,75] At lower temperatures, the isotopic range of Nb_2C is relatively narrow, while NbC fluctuates from $NbC_{0.70}$ to $NbC_{0.99}$.[4] The metal atom stacking pattern in the z-phases is closely packed, with 12 layers per unit cell (ABABCACABCBC…).[76] Concerning the phase diagram of Nb–C, two major stable carbides are likely to be formed, Nb_2C and Nb–C, along with other metastable Nb–C systems.[76] These systems possess prevalent application potential due to their desired physicochemical properties, such as electrical conductivity, hardness, high melting points, and superconductivity. These carbides were previously created by directly carburizing a 20% (v/v) CH_4/H_2 mixture with B-Nb_2O_5 (niobium pentoxide). The solid-state conversion from B-Nb_2O_5 to Nb–C under temperature-programmed reaction conditions proceeded through two steps: (a) reduction to NbO_2 and (b) concurrent reduction and carburization to Nb–C.[77] On the other hand, mixing Nb metal and C powders with different C mole fractions (10–80%) using an agate mortar followed by conventional ball milling at a high speed has also been studied. When air is exposed, the mixtures are ignited spontaneously and trigger a self-propagating high temperature reaction.[78] Recently, these niobium carbides (Nb_2C and Nb–C) have mainly been investigated in experimental and theoretical modeling research as an emergent candidate of the MXene family. The initial research on Nb_2C started in 2013 with the synthesis of the Nb_2AlC ceramic phase for effective utilization as an anode for LIBs.[33] Nb_2AlC particles were etched at room temperature by soaking in aqueous hydrofluoric acid (HF). Al is removed from the mixture selectively by the HF, leaving behind OH, O, or F. The facile separation of 2D MXene layers was allowed through sonication by substituting weaker hydrogen bonds for the strong metallic bonds that connect M–A layers. The produced Nb_2C MXene has an exceptional ability to manage high charge–discharge rates and an outstanding 170 mA h g^{-1} reversible capacity at 1C. Viswanadh *et al.* demonstrated the design, phase transformation, and construction of Nb_2C phases with the help of various diffraction and electron microscopy techniques.[79] Subsequently, several reports have studied Nb–C and Nb_2C-based compounds as potential electrodes for EES applications. Specifically, the intrinsic metallic properties and distinctive geometric structures of MXenes have inspired numerous researchers to investigate their potential as anodes for sodium-ion batteries (SIBs). Hu *et al.* reported the electronic properties and ion storage capabilities, including sodium-ion storage of Nb_2C monolayers and their derivatives based on first principle calculations.[80] Fig. 4a and b represent the triple layer constructed in the order Nb(1)–C–Nb(2) that makes up each bare Nb_2C monolayer. This triple layer can be considered as two Nb-atomic layers, cleaved with one C-atomic layer to

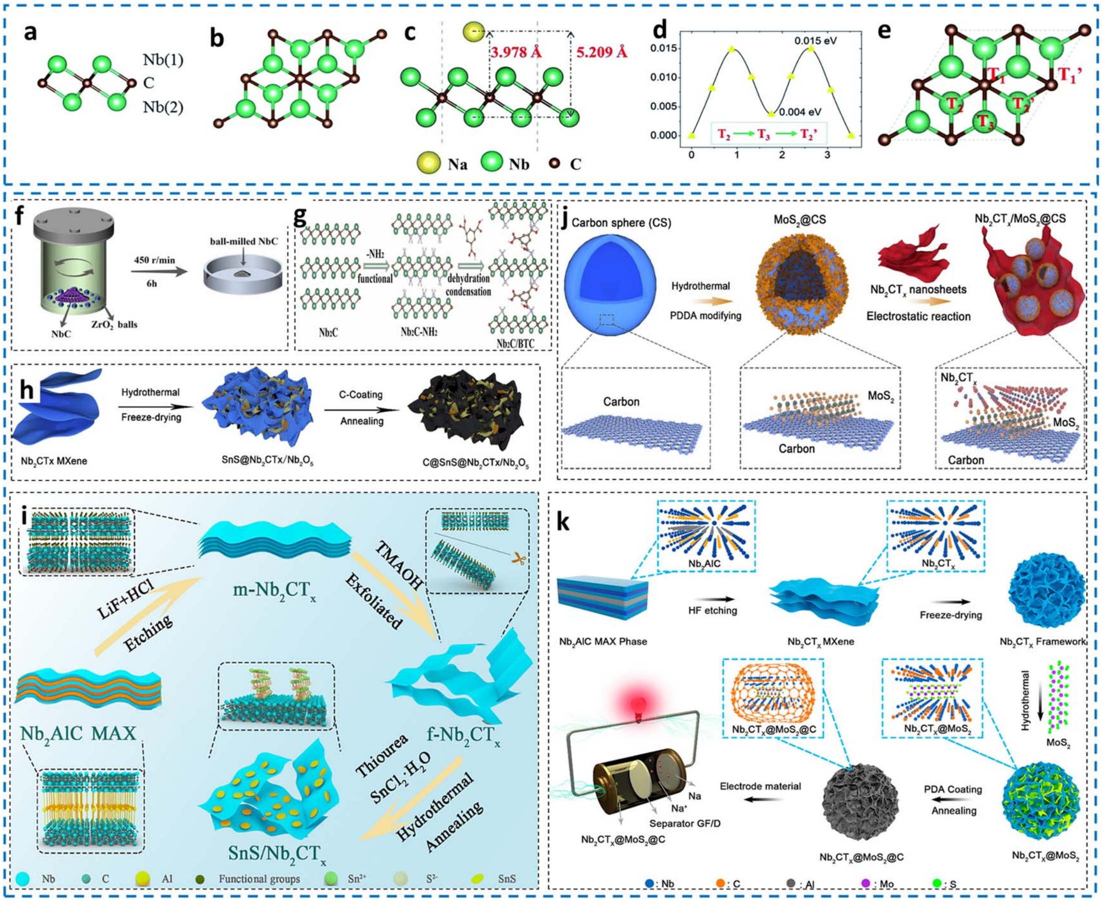

Fig. 4 (a) Side view and (b) top view of the bare Nb_2C monolayer consisting of a triple atomic layer with the Nb(1)–C–Nb(2) stacking sequence, (c) side view of Nb_2C after adsorption with Na, (d) diffusion barrier of Na on Nb_2C, and (e) identification of the high symmetry spots on the diffusion routes, reproduced with permission from ref. 80, Copyright 2016, Royal Society of Chemistry. Schematic annotations for the different preparation processes of (f) ball-milled Nb–C, reproduced with permission from ref. 81, Copyright 2021, Wiley. (g) Amino-functionalized Nb_2C, reproduced with permission from ref. 82, Copyright 2022, Elsevier. (h) The $C@SnS@Nb_2CT_x/Nb_2O_5$ hybrid; (i) the etching, exfoliation, and hydrothermal processes from the Nb_2AlC MAX phase to the SnS/Nb_2CT_x process, reproduced with permission from ref. 83, Copyright 2023, Elsevier. (j) $Nb_2CT_x/MoS_2@CS$ and (k) the 3D $Nb_2CT_x@MoS_2@C$ hybrid, reproduced with permission from ref. 84, Copyright 2022, Elsevier.

produce edge-shared Nb_2C octahedra. Fig. 4c shows Na adsorbed Nb_2C monolayers, where the distances between Nb(2) and Na and between Nb(2) and C are 5.209 and 3.978 Å, respectively. This has been reflected in the charge transfer during the adsorption process, where the Na atom transfers a charge of about 0.68e, indicating that the adsorption of Na atoms on Nb_2C facilitates redox reactions like other electrode materials. Further, the Na-ion diffusion profile and their diffusion path are presented in Fig. 4d and e, respectively. The calculated energy barrier for Na-ion diffusion was 0.015 eV, and their diffusion migrates from T_2 to $T_2^{'}$ sites through the T_3 site. This low diffusion energy barrier height demonstrated their facile Na-ion diffusion on the Nb_2C monolayer, which is one of the important characteristics in energy storage systems. In the context of SIBs, a key report on Nb–C was presented by Wang *et al.*, who prepared Nb–C with the ball-milling approach (Fig. 4f).[81] A specific amount of bulk Nb–C was milled using $Zr–O_2$ balls with a uniform size at 450 rpm for 6 hours to produce ball-milled NbC. Subsequent research was conducted using niobium-based two-dimensional MXenes. Du *et al.* used a simple hydrothermal method at 80 °C for 24 hours, followed by washing and freeze-drying the products, to synthesize Nb_2CT_x MXene, which promoted high Nb valence creation.[27] Liu *et al.* proposed a molecular welding strategy to prepare Nb_2C/BTC hybrids with different expanded interlayer spacings with 1,3,5-benzene tricarboxylic acid (BTC) solution, where the amino-functionalized Nb_2C enables the BTC to weld into interlayers of Nb_2C chemically ().[82,85] Yuan *et al.* designed a strategy for *in situ* growth of SnS nanorods onto the Nb_2CT_x MXene framework. They decorated a 2D carbon strengthened over the SnS/Nb_2CT_x MXene ($C/SnS/Nb_2CT_x$ MXene) by a hydrothermal method, followed by annealing treatment in an inert atmosphere (Fig. 4h).[86] Before this, the MAX phase was treated with concentrated HF acid (50%) to produce exfoliated few layers of Nb_2CT_x MXene. On the other hand, Wang *et al.* proposed SnS decoration over Nb_2CT_x MXene by a facile solvothermal and subsequent annealing treatment (Fig. 4i).[83] Here, the Al layer from the MAX phase was removed using hydrochloric acid and lithium fluoride solution (9 M HCl/1 g LiF) at ambient temperature for 90 hours, followed by centrifugation and freeze drying to form multi-layered m-Nb_2CT_x MXene. This m-Nb_2CT_x MXene was converted to few-layered MXenes (f-Nb_2CT_x MXene) by intercalation/delamination with tetramethylammonium hydroxide (TMAOH) at room temperature. The prepared f-Nb_2CT_x MXene facilitates the uniform *in situ* growth of SnS nanoparticles by solvothermal and annealing processes with specified precursors. Notably, instead of deionized water, ethanol was used as the solvent for the solvothermal synthesis of SnS/Nb_2CT_x to avert the Nb_2CT_x MXene's oxidation, thereby preserving its outstanding metallic conductivity, which enhances the overall sodium performance of SnS/Nb_2CT_x. Similarly, Yuan *et al.* designed a hierarchical structure comprising carbon sphere-supported Nb_2CT_x MXene/MoS_2 through a facile hydrothermal and electrostatic self-assembly process (Fig. 4j), where the MoS_2 carbon sphere acted as the support medium, and Nb_2CT_x sheets successfully prevent MoS_2 shedding-related capacity reduction, thereby shortening the sodium-ion diffusion paths and enhancing cycling and rate performance.[84] The same group developed a robust three-dimensional Nb_2CT_x@MoS_2@C cross-linked structure through multi-layered MAX phase to few-layered MX structures (Fig. 4k).[87] Few layered structures were obtained through the hydrothermal approach using TMAOH at 140 °C for 24 hours with the addition of ascorbic acid. Through a hydrothermal reaction, the many functional groups on the Nb_2CT_x MXene structure may interact with the MoS_2 nanosheets to generate an excellent 3D cross-linked hybrid architecture that inhibits the restacking of MoS_2 sheets. The high chemical catalytic activity of Nb_2CT_x MXene stems from its abundance of active groups. MoS_2 materials readily react with the surface functional groups of Nb_2CT_x MXene to produce composites. Furthermore, the Nb_2CT_x MXene surface's –OH group exhibits strong hydrophilicity, offering a multitude of anchor sites that facilitate homogeneous MoS_2 growth on the surface. In all the MXene exfoliation processes, freeze-drying is crucial because it helps preserve the structure and properties of the exfoliated nanosheets. During freeze-drying, water or other solvents are removed from the exfoliated MXene under low temperatures and reduced pressure, preventing individual layers' re-stacking. This method maintains the high surface area and prevents the oxidation and degradation of MXenes, which can occur with other drying methods. Additionally, freeze drying ensures that the functional groups and the overall morphology of the MXene are preserved, leading to better sodium storage performance.

3.2. Structural and electrochemical behaviors of niobium carbide-based MXenes

This section potentially elaborates on the various physicochemical properties and electrochemical performances of niobium-based MXenes in detail. As shown in Fig. 5a and b, the XRD pattern showed that the prepared Nb–C is in the cubic phase with the space group $Fm\bar{3}m$ (PDF 89-3830), without noticeable impurities.[27,81] Each peak from ball-milled Nb–C was slightly broader than that of bulk Nb–C, signifying the reduction in particle size after the high-energy ball-milling approach. Similarly, three broad Raman peaks have been noticed, which correspond to the Nb–C system's internal vibration modes.[88] The corresponding FE-SEM micrographs of the bulk and ball-milled Nb–C, as shown in Fig. 5h, clearly demonstrated the significant reduction in the particle size from microparticles (2–5 μm) of bulk to nanoparticles (160–480 nm) of ball-milled Nb–C, respectively.[81] This is reflected in the Nb–C's surface area increasing from 1.0 to 13.2 $m^2\ g^{-1}$ following the ball-milling process. The enhanced surface area promotes Na^+ transfer and limits side reactions at the electrolyte–electrode interface. These supportive structural and textural properties of ball-milled Nb–C facilitate reversibility in the subsequent cycles after developing the solid–electrolyte interface (SEI) at the electrode surface. Before etching, the raw material, the MAX phase of Nb_2AlC, showed well crystalline peaks in the standard pattern (JCPDS No. 30-0033). After HF etching, the sharp peaks are slightly broadened with a significant reduction in the intensity. In addition, a Nb_2AlC layered structure's characteristic peak of the (002) crystal plane at 12.6° was shifted towards a lower angle of 10° (corresponding to a lattice space of 0.78 nm), confirming the formation of Nb_2CT_x MXene with good exfoliation.[89] The unique layered structure of the MXene made up of neatly stacked Nb_2CT_x flakes with a thickness of around 25 nm was clearly visible in the Nb_2CT_x SEM images (Fig. 5i).[27] These flakes are most likely thermally exfoliated graphite. The XRD patterns of long-term HF etching have been presented in Fig. 5c for $Nb_4C_3T_x$ – 10 days, $Nb_4C_3T_x$ – 5 days, $Nb_{3.5}Ta_{0.5}C_3T_x$ – 5 days, and $Nb_{3.9}W_{0.1}C_3T_x$ – 5 days. It is evident that all samples' prominent peaks lost some of their intensity during etching, which signifies that Al was eliminated during the etching process.[26] The existence of (Nb, W)C in the W5 sample is the cause of the unreacted (Nb, W)C indicated by black dots. The amine-functionalized Nb_2C (2-Nb_2C/BTC, 6-Nb_2C/BTC, 12-Nb_2C/BTC, and Nb_2C) exhibits a low angle shift of (002) diffraction peaks at 7.07°, 7.10°, 7.21°, and 7.66°, which correspond to the interlayer spacing of 1.250 nm, 1.246 nm, 1.227 nm, and 1.026 nm, respectively (Fig. 5d).[82] This was observed in the FE-SEM images (Fig. 5l(i–iv)), where the layer space was significantly large after amino-functionalization compared to the bulk MXenes.[82] As presented in Fig. 5e(i), the etching of Al layers with TMAOH is confirmed by vanishing the (103) peak at around 38.7°.[83] Furthermore, when comparing m-Nb_2CT_x to Nb_2AlC, there is a clear leftward shift of the (002) peak, which suggests that the Al layer removal has increased interlayer spacing. The (002) diffraction peak of the few-layered Nb_2CT_x MXene exhibits a minor leftward shift, signifying the subsequent interlayer spacing expansion and transition from m-Nb_2CT_x MXene to very few-layered Nb_2CT_x MXene. Fig. 5f(ii) shows the XRD patterns of the target SnS/Nb_2CT_x MXene, where all the characteristic peaks of SnS attributed to the orthorhombic phase, along with the (002) plane of Nb_2CT_x MXene at a lower angle, confirm the balanced composition of SnS and Nb_2CT_x MXene.[84] The morphology of Nb_2CT_x MXene discloses its wrinkled ultrathin sheet (Fig. 5k(i)) and even nucleation of SnS over the surface of Nb_2CT_x MXene from the stacked bulk to nanoparticles (Fig. 5k(ii)).[87] Similarly, introducing Nb_2CT_x MXene into the MoS_2@carbon spheres makes the plane (002) shift from 13.0° to 8.9° and 5.7° to left after etching and

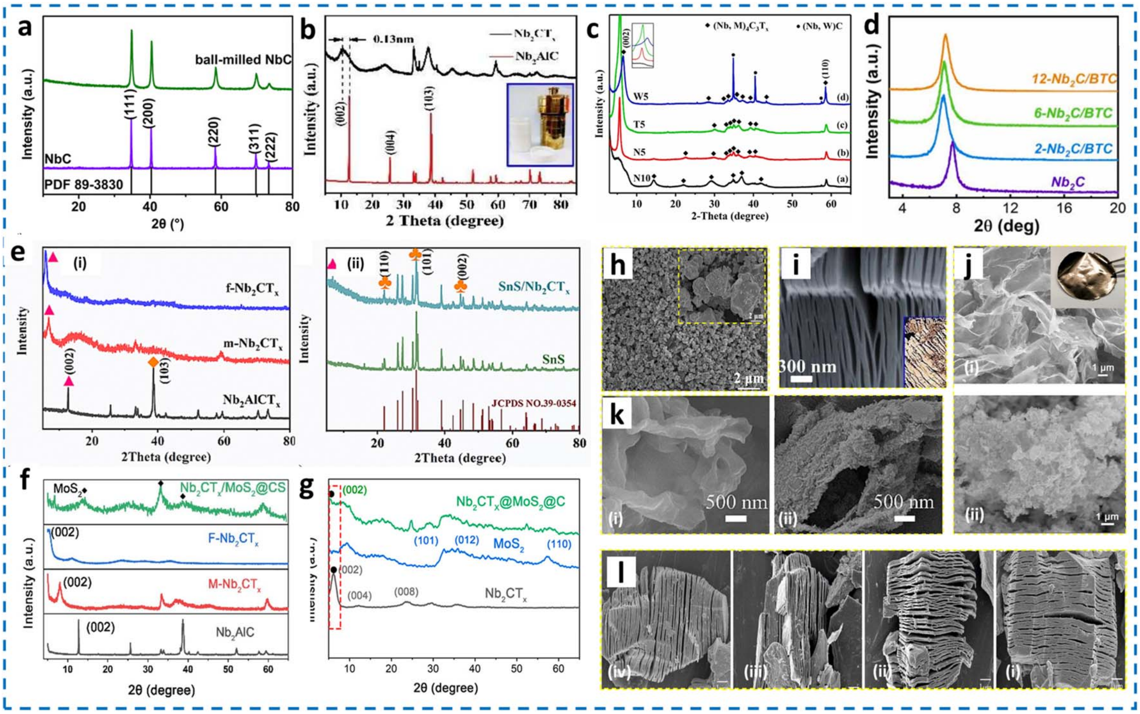

Fig. 5 (a) XRD patterns and (h) FE-SEM images of bulk and ball-milled NbC, reproduced with permission from ref. 81, Copyright 2021, Wiley. (b) XRD pattern of Nb_2AlC before and after HF etching; (i) FE-SEM image of Nb_2CT_x (after HF etching), reproduced with permission from ref. 27, Copyright 2020, Wiley. (c) XRD patterns of post-HF-treatment at different etching timings [(a) $Nb_4C_3T_x$ – 10 days; (b) $Nb_4C_3T_x$ – 5 days, (c) $Nb_{3.5}Ta_{0.5}C_3T_x$ – 5 days, and (d) $Nb_{3.9}W_{0.1}C_3T_x$ – 5 days], reproduced with permission from ref. 26, Copyright 2019, Elsevier. (d) XRD pattern (l) of bare Nb_2C and Nb_2C-BTCs by molecular welding, reproduced with permission from ref. 82, Copyright 2022, Elsevier. (e) XRD patterns and (k) FE-SEM images of Nb_2AlCT_x, multi- and few-layered Nb_2CT_x (i), and the SnS introduction to Nb_2CT_x (ii) by the hydrothermal approach, reproduced with permission from ref. 83 and 87, Copyright 2023, Elsevier, and Copyright 2021, The American Chemical Society. (f) XRD pattern of the Nb_2CT_x/MoS_2@carbon spheres and their controlled samples, reproduced with permission from ref. 84, Copyright 2022, Elsevier. (g) XRD pattern and (j) FE-SEM images before and after the addition of MoS_2 into the Nb_2CT_x nanosheets, reproduced with permission from ref. 87, Copyright 2021, The American Chemical Society.

delamination (Fig. 5f).[84] Meanwhile, a similar shift has been observed in the Nb_2CT_x@MoS_2@C hybrid after the MoS_2@C addition into the Nb_2CT_x MXene framework (Fig. 5g) and the corresponding FE-SEM images (Fig. 5j(i) and (ii)) indicate the formation of a 3D crosslinked morphology in the Nb_2CT_x@MoS_2@C hybrid.[87]

The high-resolution microscopy images are an important tool for identifying the nature and interlayer spacing of the prepared MXenes. Fig. 6a(i) and (ii) present the HR-TEM images of the SnS/Nb_2CTx hybrid structure at different magnifications, in which the size of the SnS particles is around 30 nm anchored onto the MXene nanosheets.[83] The experimental interlayer spacing is 0.29 nm and 0.34 nm, belonging to the (101) and (120) planes of orthorhombic SnS. The clear selected area diffraction pattern (SAED) rings are attributed to the (011), (002), and (020) planes of orthorhombic SnS as presented in the inset of Fig. 6a(i) and (ii). The deconvoluted Nb 3d core-level spectrum also identified the emergence of Nb–O–Sn and Nb–S peaks at 210.3 eV and 209.2 eV bonds, demonstrating the strong coupling of SnS with Nb_2CT_x MXene (Fig. 6b).[83] The initial three cycles of cyclic voltammetry (CV) curves of the SnS/Nb_2CT_x hybrid electrode at 0.2 F g^{-1} s^{-1} are presented in Fig. 6c.[85] It depicted a single irreversible reduction peak (0.55 V) corresponding to the formation of the SEI, which vanished from the second cycle. From the 2nd sweep, the Na^+ intercalation into the SnS is correlated by a broad peak in the voltage ranges of 1.0 V and 0.6 V, respectively, and the subsequent multistep alloy reaction that creates Na_xSn. Regarding the anodic scan, the stepwise dealloying reaction of Na_xSn is represented by the peak at 0.71 V. The succeeding oxidation phase is defined by the peaks from 1.1 to 1.6 V. Consistent with the CV curves, the initial cycles of galvanostatic charge–discharge curves reflected similar voltage plateaus at 0.1 A g^{-1} (Fig. 6d). Based on reactions, the sodium storage process of SnS can be illustrated as follows:[91,92]

$$SnS + 2Na^+ + 2e^- \leftrightarrow Sn + Na_2S \quad (1)$$

$$Sn + xNa^+ + xe^- \leftrightarrow Na_xSn \quad (2)$$

Moreover, the initial sodiation and de-sodiation capacities of SnS/Nb_2CT_x hybrid electrodes are 744.1 and 408.5 mA h g^{-1} with an initial coulombic efficiency of ∼55%. Fig. 6e further compares the cycling performance of the Nb_2CT_x, pure SnS, and SnS/Nb_2CT_x electrodes at 0.1 A g^{-1}. Specifically, the SnS/Nb_2-

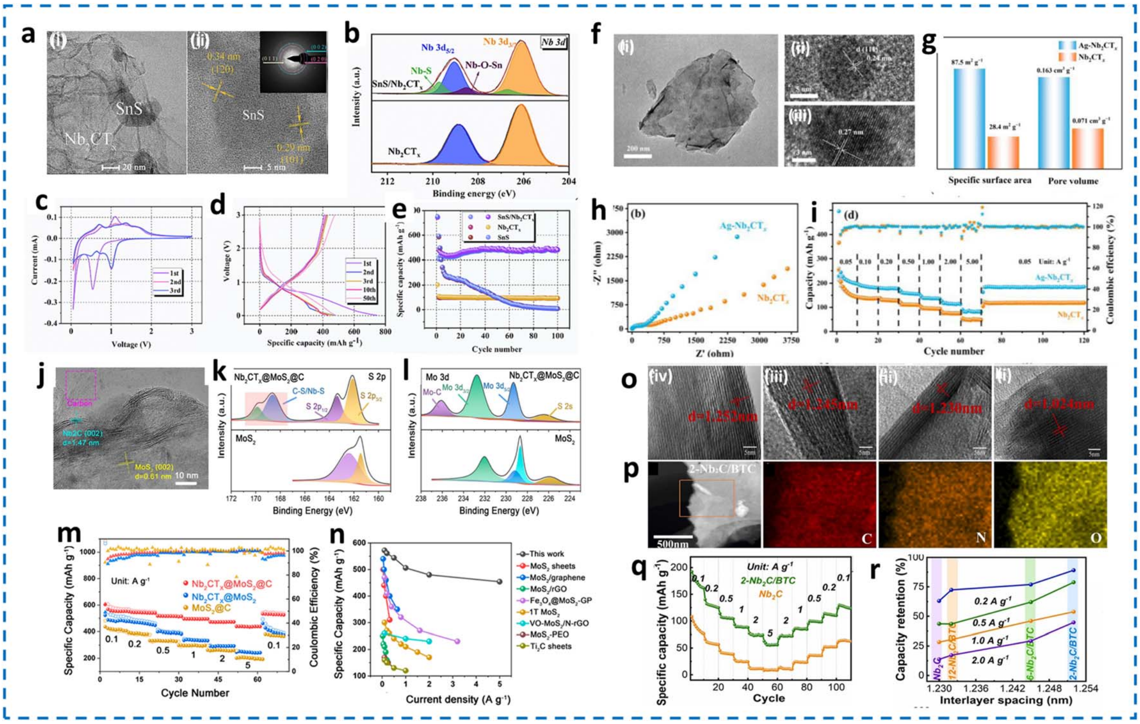

Fig. 6 (a) HR-TEM images of the SnS@Nb_2CT_x nanosheets at (i) 20 nm and (ii) 5 nm scale bar, (b) Nb 3d core-level spectrum of pristine Nb_2CT_x and SnS/Nb_2CT_x, (C) CV curves @ 0.2 mV s^{-1}, (d) GCD curves @ 0.1 A g^{-1} for the initial cycles of SnS/Nb_2CT_x, and (e) cycling stability curves for bare and SnS/Nb_2CT_x electrodes, reproduced with permission from ref. 83, Copyright 2023, Elsevier. (f) TEM image of Ag–Nb_2CT_x (i), HR-TEM image of Ag NPs (ii) and Nb_2CT_x nanosheets (iii), (g) comparison of specific surface areas and pore volumes, (h) Nyquist plot and (i) rate stability at various current densities of bare and Ag infused Nb_2CT_x nanosheets, reproduced with permission from ref. 90, Copyright 2022, Elsevier. (j) HRTEM images of Nb_2CT_x@MoS_2@C, (k) S 2p core-level and (l) Mo 3d core-level spectra of bare MoS_2 and Nb_2CT_x@MoS_2@C, (m) rate capability at various current densities and (n) specific capacity comparison with MoS_2 based electrodes, reproduced with permission from ref. 87, Copyright 2021, The American Chemical Society. (o) HR-TEM images of Nb_2C (i), 2-Nb_2C/BTC (ii), 6-Nb_2C/BTC (iii), and 12-Nb_2C/BTC (iv), (p) elemental mapping of 2-Nb_2C/BTC, (q) rate capability curve at different current densities and (r) capacity retention concerning the interlayer spacing for Nb_2C/BTC electrodes, reproduced with permission from ref. 82, Copyright 2022, Elsevier.

CT_x electrode exhibits its high sodium storage activity by maintaining the maximum capacity of approximately 479.6 mA h g^{-1} after 100 cycles, which is higher than that of bare Nb_2CT_x MXene (93.3 mA h g^{-1}) and SnS (8.5 mA h g^{-1}). Fig. 6f shows the TEM and HR-TEM images of the introduction of Ag nanoparticles over the ultrathin atomic sheet-like structure of Nb_2CT_x (with a lateral size of 500–1000 nm).[90] The Ag NPs closely linked to the Nb_2CT_x nanosheets have a dimension of around 5–20 nm, and the 0.24 nm fringe spacing matches the Ag (111) plane's spacing (Fig. 6f). The anchoring of the Ag nanoparticles to Nb_2CT_x has drastically enhanced the specific surface area and pore volume (Fig. 6g) to 87.5 m^2 g^{-1} and 0.163 cm^3 g^{-1} compared to pure Nb_2CT_x. This could decrease the charge transfer resistance and enhance the sodium ion diffusion kinetics, as evidenced by the Nyquist plot (Fig. 6h). The rate performance at various current densities ranging from 50 mA g^{-1} to 5 A g^{-1} is revealed for pure and Ag–Nb_2CT_x electrodes in Fig. 6i. The Ag–Nb_2CT_x electrode exhibits superior sodium-ion storage capacity at varying current intensities; at 0.05 A g^{-1}, its specific capacity is 185 mA h g^{-1}, and it continues to remain at 86 mA h g^{-1} even when the current density is increased by 100 times to 5.00 A g^{-1}. The HR-TEM image of MoS_2 incorporation in Nb_2CT_x@MoS_2@C MXenes is shown in Fig. 6j, in which the (002) planes of Nb_2C and MoS_2 are confirmed by the interlayer distances of 1.47 nm and 0.61 nm, respectively.[87] Similar to the SnS incorporation, Nb_2C core-level comparison analysis shows that Nb $3d_{3/2}$ and Nb $3d_{5/2}$ were slightly shifted toward the higher binding energy in Nb_2CT_x@MoS_2@C hybrid structures than pure Nb_2CT_x, resulting in the expansion of the MoS_2 nanosheet altering the electron distribution of Nb 3d. The appearance of Nb–S, Mo–C, and C–S bonds in the S 2p (Fig. 6k) and Mo 3d (Fig. 6l) core-level spectra signifies the generation of strong coupling between MoS_2 and pure Nb_2CT_x in Nb_2CT_x@MoS_2@C hybrid structures. According to the CV curves of the Nb_2CT_x@MoS_2@C hybrid electrode (Fig. 6m), the electrochemical reaction mechanisms with the sodium storage process can be explained as follows:

$$MoS_2 + xNa^+ + xe^- \rightarrow Na_xMoS_2 \tag{3}$$

$$Na_xMoS_2 + (4 - x)Na^+ + 4e^- \rightarrow Mo + 2Na_2S \tag{4}$$

$$Nb_2CT_x + yNa^+ + ye^- \rightarrow Na_yNb_2CT_x \tag{5}$$

These factors facilitate the high-rate performance of Nb_2CT_x@MoS_2@C hybrid structures, resulting in retained specific

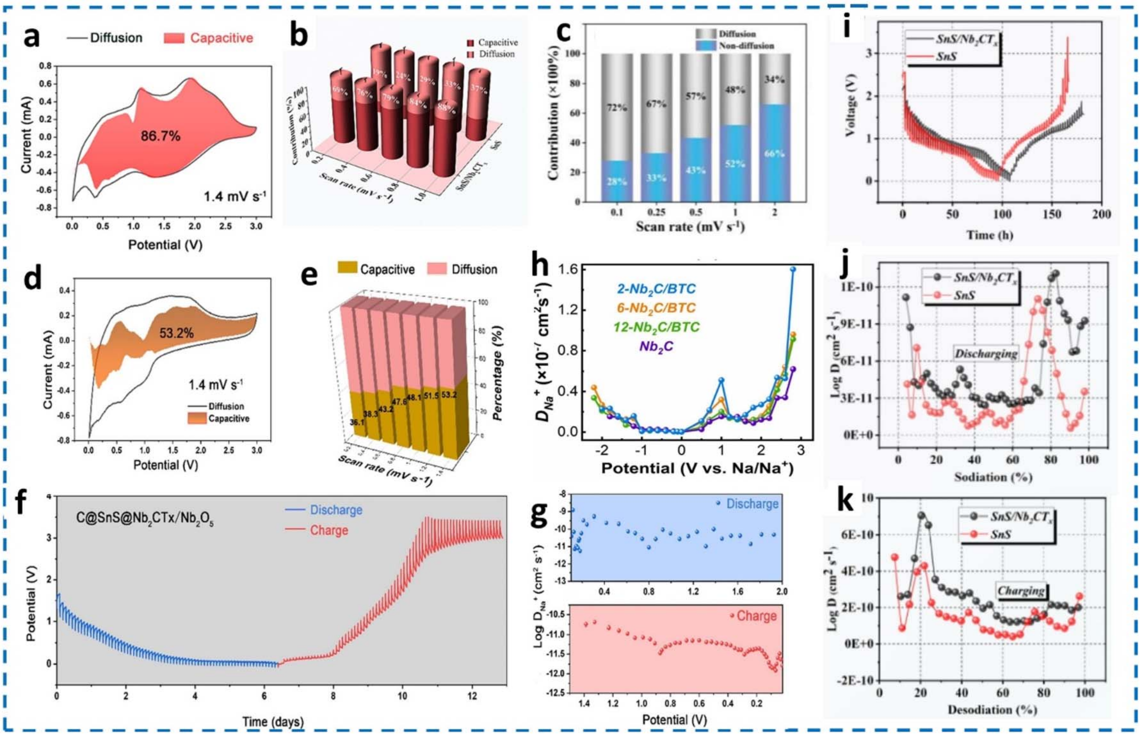

Fig. 7 Electrode kinetic mechanisms: capacitive contribution in the CV curve for (a) the Nb_2CT_x@MoS_2@C electrode, reproduced with permission from ref. 84, Copyright 2022, Elsevier. (d) Capacitive contribution in the CV curve for C@SnS@Nb_2CT_x/Nb_2O_5 at 1.4 mV s^{-1}, percentage contributions of capacitive and diffusion processes for (b) SnS, reproduced with permission from ref. 83, Copyright 2022, Elsevier. Percentage contributions of capacitive and diffusion processes for SnS@Nb_2CT_x electrodes, reproduced with permission from ref. 83, Copyright 2023, Elsevier. (c) Ag–Nb_2CT_x electrode, reproduced with permission from ref. 90, Copyright 2022, Elsevier. (e) C@SnS@Nb_2CT_x/Nb_2O_5 at various scan rates. (f) GITT curves and (g) corresponding D_{Na^+} values at charge and discharge states of the C@SnS@Nb_2CT_x/Nb_2O_5 electrode, reproduced with permission from ref. 83, Copyright 2022, Elsevier. (h) D_{Na^+} values of bare Nb_2C and Nb_2C/BTC electrodes, (i) GITT curves, and D_{Na^+} values of (j) discharging and (k) charging states for bare SnS and SnS/Nb_2CT_x electrodes, reproduced with permission from ref. 83 and reproduced with permission from ref. 83, Copyright 2023, Elsevier.

capacities of 572, 561, 544, 506, 480, and 454 mA h g^{-1} at the current densities of 0.1, 0.2, 0.5, 1, 2, and 5 A g^{-1}, respectively (Fig. 6n). HRTEM images, as displayed in Fig. 6o(i)–(iv), can be used to further confirm the 2D layered structure of Nb_2C/BTC.[82] The observed interlayer distances of 1.252, 1.245, 1.230, and 1.024 nm for 2-Nb_2C/BTC, 6-Nb_2C/BTC, 12-Nb_2C/BTC, and Nb_2C, respectively, which are observed by the XRD results as shown in Fig. 6l. The obtained interlayer distance value demonstrates the anchoring effects of the BTC molecules welded into the Nb_2C layers. The discharge capacity of the optimized Nb_2C/BTC electrode was 164.0 mA h g^{-1} at 0.1 A g^{-1}, which is almost twice that of the bare Nb_2C electrode (78 mA h g^{-1}). 53.8% and 28.3% capacity retentions were obtained from 0.1–1.0 A g^{-1} for 2-Nb_2C/BTC and bare Nb_2C electrodes, respectively (Fig. 6q and r). Further, the higher sodium ion diffusion coefficient of 2-Nb_2C/BTC than that of other components demonstrated its superior diffusivity during charge–discharge analysis.

3.3. Electrochemical kinetics and theoretical studies of niobium carbide-based MXenes

The electrochemical kinetics of the MXene electrodes were mainly investigated using the analysis of capacitive/diffusion contributions and the galvanostatic intermittent titration technique (GITT). The capacitive contributions can generally be derived from the power law [$i = a \times v^b$ ($0.5 \le b \le 1$)] and the following plot of the logarithmic scale of scan rate *vs.* current densities ($\log v$ *vs.* $\log i$), where 'i' is the responsive current (A) and 'v' is the sweep rate (mV s^{-1}). A capacitive behavior (surface-controlled processes) has a slope (b) of 1.0, whereas diffusion behavior (diffusion-controlled processes) has a slope (b) of 0.5. Further modification transforms the equation to [$i = k_1v + k_2v^{1/2}$], where k_1v is the surface and $k_2v^{1/2}$ is the diffusive controlled processes, respectively. Fig. 7a shows the CV curves of the Nb_2CT_x@MoS_2@C hybrid anode at 1.4 mV s^{-1} separating with the capacitive contribution of 86.7%,[86] whereas the C@SnS@Nb_2CT_x/Nb_2O_5 hybrid anode delivered only 53.2% (Fig. 7d).[87] These surface-dominated reaction contributions were significantly reduced to 69.9 and 36.1% for the same electrodes at a lower sweep rate of 0.2 mV s^{-1} (Fig. 7e). A two-dimensional layered structure in the skeleton (Nb_2CT_x) and active materials (MoS_2@C) in the Nb_2CT_x@MoS_2@C hybrid anode facilitates enhanced surface-controlled reactions. In contrast, two-dimensional SnS_2 was converted to the most stable form of SnS after the annealing process with a low level of Nb_2O_5, leading to mixed controlled reaction mechanisms in the

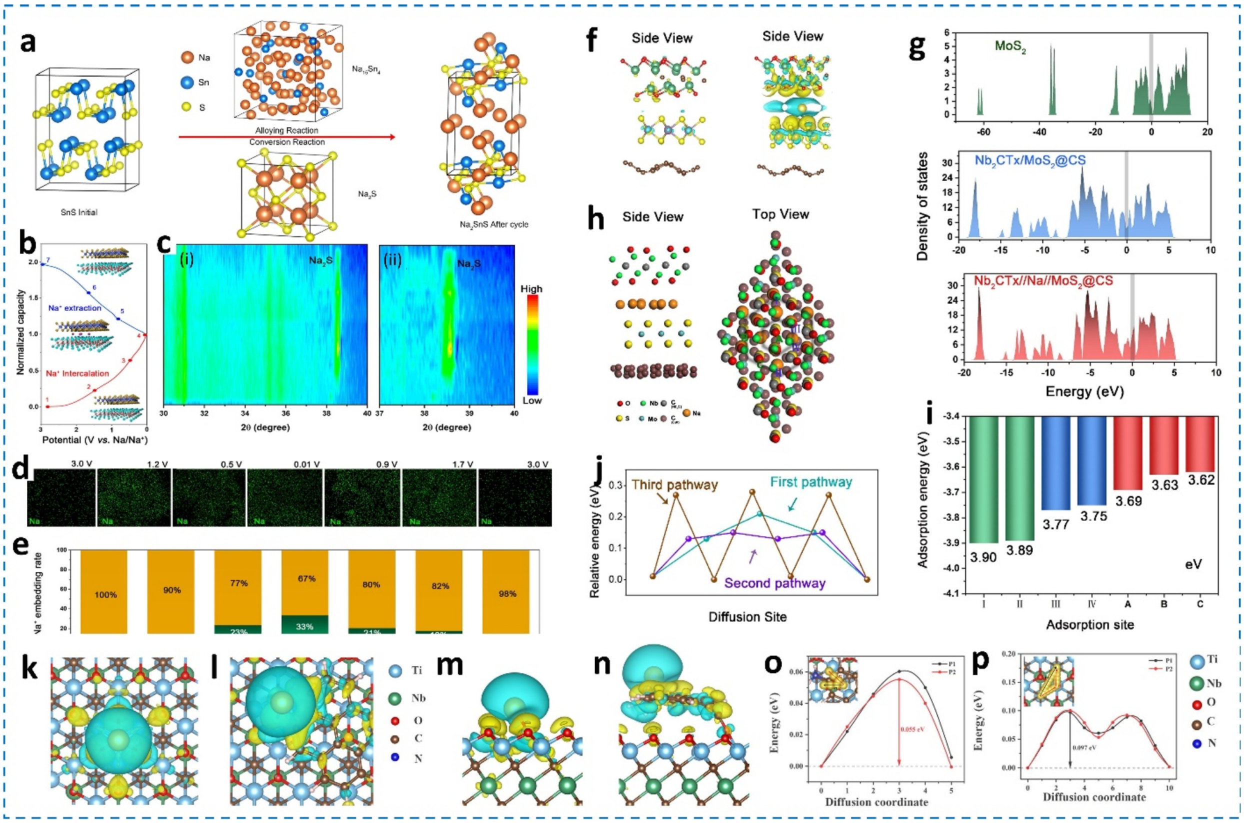

Fig. 8 (a) The schematic diagram of SnS evolution in the C@SnS@Nb_2CT_x/Nb_2O_5 electrode, reproduced with permission from ref. 86, Copyright 2022, Elsevier. (b) Charge and discharge profiles of the Nb_2CT_x@MoS_2@C electrode at 0.01–3.0 V, (c) contour maps of *in situ* synchrotron X-ray diffraction collected during the 1st charge and discharge, (d) mapping image of the sodiated electrode, and (e) sodium-ion intercalation rate at different voltage intervals as marked in (b), reproduced with permission from ref. 87, Copyright 2021, The American Chemical Society. Simulation analysis: (f) charge density variations of Nb_2CT_x/MoS_2@CS before and after the intercalation of sodium, (g) density of states (DOS) of MoS_2, Nb_2CT_x/MoS_2@CS and Nb_2CT_x//Na//MoS_2@CS, (h) sodium adsorbed sites of Nb_2CT_x/MoS_2@CS, (i) 3-different paths of the relative energy change curve, and (j) different Na adsorbed sites' adsorbed energies, reproduced with permission from ref. 84, Copyright 2022, Elsevier. The top and side views of the charge–density difference for Na adsorbed on (k and l) $Ti_2NbC_2T_x$ and (m and n) $Ti_2NbC_2T_x$@CDs, and Na-ion diffusion routes and corresponding Na-ion diffusion energy barriers on (o) $Ti_2NbC_2T_x$; (p) $Ti_2NbC_2T_x$@CDs, reproduced with permission from ref. 94, Copyright 2024, Elsevier.

C@SnS@Nb_2CT_x/Nb_2O_5 electrode. Fig. 7b displays the capacitive and diffusion contributions of the pure SnS and SnS/Nb_2CT_x electrodes from various scan rates. The capacitive contribution of the SnS/Nb_2CT_x electrode with respect to the total capacity is calculated to be 88.2% at 1.0 mV s^{-1} and 69.0% at 0.2 mV s^{-1}, whereas pure SnS delivered only 36.6% at 1.0 mV s^{-1}, which revealed the anchoring of SnS onto the Nb_2CT_x nanosheets and enhanced reaction kinetics. Similarly, the Ag-anchored Nb_2CT_x electrode displayed enhanced capacitive contributions from 28% to 66% (0.1 to 2 mV s^{-1}), which will accelerate the connection of sodium ions to the active site and improve the reaction kinetics (Fig. 7c). The other vital parameters of reaction kinetics are the diffusion coefficient of sodium ions (D_{Na^+}) calculated using Ficks' second law [$D_{Na^+} = 4\pi t (m_B V_M/M_B S)^2 \times (\Delta E_s/\Delta E_t)^2$] using GITT measurements,[93] where t denotes the pulse time; total contact area between the electrolyte and electrode is denoted by S; V_M, m_B and M_B are the molar volume, the mass and the molar weight of the active materials, respectively; and ΔE_s and ΔE_t are differences in the steady-state potential after deducting the IR-drop and total transient change in the cell voltage during a single titration, respectively. The (D_{Na^+}) values of bare Nb_2C, 2-Nb_2C/BTC, 6-Nb_2C/BTC, and 12-Nb_2C/BTC electrodes were compared and presented in Fig. 7h. Fig. 7f and g display the GITT voltage profile of C@SnS@Nb_2CT_x/Nb_2O_5 and the Na^+ diffusion coefficients, respectively. The calculated range of the (D_{Na^+}) values for the C@SnS@Nb_2CT_x/Nb_2O_5 electrode is between 10^{-9} and 10^{-11}, whereas for SnS_2@C it is between 10^{-9} and 10^{-11}, signifying enhanced diffusivity. Similarly, the GITT curves (Fig. 7i) and corresponding (D_{Na^+}) at sodiation (Fig. 7j) and de-sodiation states (Fig. 7k) for pure SnS and SnS/Nb_2CT_x electrodes have been determined.[83] Upon initial discharge, the average D_{Na^+} values for the SnS/Nb_2CT_x and pure SnS electrodes are 4.31×10^{-11} and 3.27×10^{-11} cm^2 s^{-1} (Fig. 7j), respectively. Regarding the charging procedure, the corresponding D_{Na^+} values are 2.56×10^{-10} and 1.62×10^{-10} cm^2 s^{-1} (Fig. 7k), indicating that the redox kinetics of the charging process are more favorable. The SnS/Nb_2CT_x electrode's Na^+ diffusion coefficients are higher than those of SnS in all voltage ranges, demonstrating the structural benefits brought about by the addition of Nb_2CT_x MXene.

Table 1 Electrochemical and cycling performances of various niobium carbide-based anodes for SIBs

Electrode material	Synthesis strategy	Electrolyte	Initial coulombic efficiency (%)	Cycling stability (mA h g^{-1})	Rate capability (mA h g^{-1})	Reference
Bulk Nb–C	Ball milling	1 M $NaPF_6$ in diglyme	77	110 (40 cycles)	83 (5 A g^{-1})	81
Ball-milled Nb–C			79	262 (40 cycles) @ 0.1 A g^{-1}	160 mA h g^{-1} (40 cycles)	
Nb_4AlC_3	Hot press sintering	1 M $NaClO_4$ in PC with 5% FEC	31	—	—	26
$Nb_{3.5}Ta_{0.5}AlC_3$			39.8			
$Nb_{3.9}W_{0.1}AlC_3$			24			
Nb_2CT_x MXene	Selective etching	1 M $NaClO_4$ in EC/DMC (1 : 1) with 10% FEC	42.9	102 (500 cycles) @ 1 A g^{-1}	99 (2 A g^{-1})	27
Nb_2C	Dehydration condensation reaction	1 M $NaPF_6$ in EC : DC : DMC	—	55 (130 cycles)	22.1 (1 A g^{-1})	82
Nb_2C/BTC			—	109.7 (130 cycles) @ 0.1 A g^{-1}	88.1 (1 A g^{-1})	
C@SnS@Nb_2CT_x/Nb_2O_5	Hydrothermal and annealing	1 M $NaClO_4$ in EC/DEC (1 : 1) with 5% FEC	44	384 (100 cycles) @ 0.1 A g^{-1}	240 (5 A g^{-1})	86
Nb_2-CT_x MXene	Solvothermal and annealing	1 M $NaClO_4$ in EC/PC (1 : 1) with 5% FEC	49.1	93.5% (100 cycles)	—	83
SnS/Nb_2CT_x MXene			54.9	479.6 (100 cycles) @ 0.1 A g^{-1}	191.6 (5 A g^{-1})	
Nb_2CTx@MoS_2	Freeze-drying and hydrothermal	1 M $NaClO_4$ in EC/DC (1 : 1) with 5% FEC	49	161 (200 cycles)	—	87
Nb_2CT_x@MoS_2@C			58	530 (200 cycles) @ 0.1 A g^{-1}	454 (200 cycles) @ 5.0 A g^{-1}	
$Ti_2NbC_2T_x$@CDs	Etching and hydrothermal	1 M $NaPF_6$ in EC : DMC (1 : 1) with 5% FEC	—	109.2 mA h g^{-1} after 10 000 cycles at 5 A g^{-1}	>100 mA h g^{-1} (10 A g^{-1})	94

Ex situ and simulation studies are essential for validating the results and investigating the reaction mechanisms during charge and discharge.[86] Fig. 8a demonstrates the schematic annotation of SnS evolution in the first cycle process, which was speculated through the *ex situ* analysis of C@SnS@Nb_2CT_x/Nb_2O_5. Alloying and conversion reactions can be used to wrap up this reaction. While the conversion reaction produced Na_2S, the alloying reaction produced $Na_{15}Sn_4$, which led to volume expansion. Moreover, the charging process could convert Sn to Na_2SnS rather than Sn to SnS. Na would be consumed as a result, impacting the initial coulombic efficiency. *In situ* synchrotron diffraction patterns were used to analyze the evolution of Nb_2CT_x@MoS_2@C at 0.01–3.0 V (Fig. 8b and c).[87] The XRD peak remains unchanged as sodium ions' intercalation and extraction process occurs, whereas the Na_2S signal appears at 38.5° in Fig. 8c. Then, the macroscopic morphology of the conversion reaction alters, and certain nanospheres emerge when sodium ions are inserted (Fig. 8d and e). The displayed elemental mapping confirmed that the appeared nanospheres mainly comprised Na and S atoms. Further, charge density variations of Nb_2CT_x/MoS_2@CS before and after sodium insertion are shown in Fig. 8f. Owing to its long transportation path, it is evident that the exchanged electrons are limited before Na insertion. In contrast, the number of electrons is plentiful after Na insertion into the lattice. While MoS_2 exhibits more of a semiconducting behavior, the DOS results (Fig. 8g) demonstrate that Nb_2CT_x/MoS_2@CS and Nb_2CT_x//Na//MoS_2@CS have greater values at the Femi position, which is consistent with charge density difference results. Four types of Na adsorption sites are identified and depicted in Fig. 8h. The calculated adsorption energies of 3.90, 3.89 eV, 3.77, and 3.75 eV for sites I, II, III, and IV, respectively, indicated that sites I and II are highly stable sites, whereas sites III and IV have a metastable nature. Furthermore, because of the Nb_2CT_x layer, sites III and IV have three symmetrical places. Several paths were chosen to identify relative energy changes based on adsorption energy (Fig. 8j). Position A is the first route. Na first visits metastable pentagon sites in the second pathway before returning to stable ones. Stable pentagon sites with energy barriers at locations B and C comprise the third route. Positions A, B, and C had adsorption energies of −3.69, −3.63, and −3.62 eV, respectively. While the second method is the simplest, adsorption energy is decreased due to the large distance between MoS_2 and Nb_2CT_x. Although III and IV are metastable and can store Na or help move it between Nb_2CT_x, Na generally stabilizes at I and II.[84] Similarly, the charge density difference between $Ti_2NbC_2T_x$ and (m, n) $Ti_2NbC_2T_x$@CDs was calculated (Fig. 8k–n). The positive charges are carried by carbon atoms in carbon dots (CDs), and Na atoms are also adsorbed on the carbon layers. The mutual repulsion between those positive charge carriers causes a lower Na-ion diffusion barrier in $Ti_2NbC_2T_x$@CDs (Fig. 8o and p). These lower diffusion barrier heights in $Ti_2NbC_2T_x$@CDs than bare $Ti_2NbC_2T_x$ are conducive to the fast transport of Na ions, facilitating better rate performance.[94] The electrochemical and cycling performances of various niobium carbide-based anodes for SIBs are tabulated in Table 1.

In addition to SIBs, aqueous sodium-ion storage ability was tested with the Nb_2C MXene composite with sodium anthraquinone-2-sulfonate (AQS) based flexible supercapacitors.[95] Before this, Nb_2C MXenes were synthesized from Nb_2AlC powder using a conventional HF etching process, and a composite with AQS was achieved using a hydrothermal method. The flexible electrode was successfully obtained using freeze-drying and vacuum methods. The presence of AQS preferably controlled the MXene aggregation, and their porous structure enhanced the ion transport between the Nb_2C layers. Therefore, the fabricated flexible supercapacitor device delivered exhibited a considerably higher electrochemical capacitance (36.3 mF cm^{-2}).[95]

4. Vanadium carbide anodes for SIBs

Due to the complexity associated with electrolyte optimization and the lack of understanding of the improvement of initial coulombic efficiency (ICE) with each electrolyte, the structural design of anode materials is believed to be a way to go for the next generation of battery materials, especially for SIBs.[38] As an anode, the new class of materials, MXenes, have attracted tremendous attention owing to their metallic-like conductivity, robustness, controllable surface functional groups such as –OH, –F, and –O, and extraordinary chemical stability.[96] However, the self-stacking in the 2D layered structure, minimal specific capacity, and insufficient ion accessibility have hampered their uses in modern applications such as SIBs. Among the numerous classes of MXenes, V_2CT_x, wherein V is vanadium, C is carbon, and T represents the surface functional groups, has shown a sizeable theoretical capacity of 940 mA h g^{-1} with other satisfactory electrochemical characteristics such as high conductivity and promising charge transfer ability.[96] Unfortunately, this class of materials has hardly been explored for their applicability to SIBs.

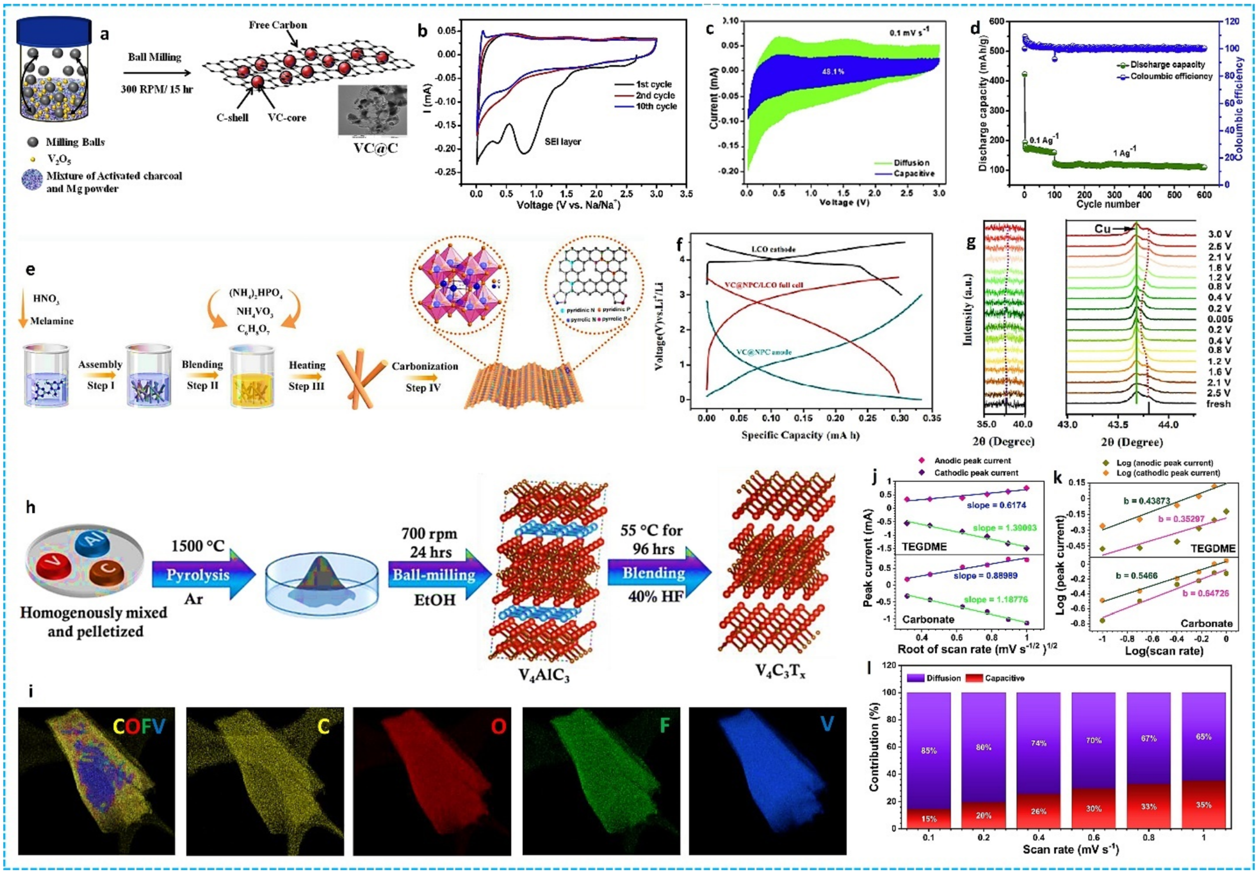

Fig. 9 (a) Graphical illustration for the preparative process of VC@C, (b) XRD pattern and (c) HR-TEM image (inset: SAED pattern) of VC@C, (d) CV at 0.2 mV s^{-1} and (e) corresponding separation curves of capacitive and diffusive behavior, and (f) cycling performance of the VC@C anode at 0.1 Ag^{-1} (100 cycles) and 1 A g^{-1} (500 cycles), and post-cycling structural studies of sodium ion half cells; (g) XRD patterns with different 2θ ranges, and (h) Raman spectrum with the zoomed-in section of the G band for the respective half-cells, reproduced with permission from ref. 97, Copyright 2020, Elsevier. (i) Typical synthesis illustration for the VC@NPC anode, (j) full cell comparison, and (k) its corresponding *ex situ* XRD pattern in the 2θ range between 35 and 40°, and 43 and 44.25° with their GCD profile, reproduced with permission from ref. 98, Copyright 2020, Elsevier. (l) Schematic diagram for the formation of V_4AlC_3 and subsequent formation of $V_4C_3T_x$, (m) TEM with the EDX profile of the proposed anode which comprises V, C, O, and F as the major constituents, (n) peak current as a function of (scan rate)$^{1/2}$ curves for $V_4C_3T_x$-T and $V_4C_3T_x$-C, (o) log I *vs.* log ν plot for $V_4C_3T_x$-T and $V_4C_3T_x$-C to determine the b value, and (p) current contribution plot including capacitive and diffusive contributions for $V_4C_3T_x$-C, reproduced with permission from ref. 99, Copyright 2023, Elsevier.

4.1. Electrochemical behaviors of vanadium carbide/carbon composite-based MXenes

In this section, we highlight some of the recent approaches to improving the electrochemical properties of vanadium carbide-based MXenes in SIBs. For instance, a carbon-coated vanadium carbide (VC@C) synthesized by using a facile, cost-effective mechano-chemical ball-milling procedure (Fig. 9a) has shown promising potential as an anode material for SIBs.[97] The formation of VC with carbon layers is confirmed by the obvious five diffraction peaks, along with the small broad peak at 26°. During milling at a high speed, VC particles agglomerate, forming interconnected structures with outer carbon layers, as inferred from HRTEM analysis (Fig. 9c). The interplanar spacings of these layers, around 0.35 nm and 0.21 nm, correspond to the (002) and (200) planes of C and VC, suitable for reversible Na ion intercalation. The SAED pattern confirms the crystalline phases of cubic VC and carbon in the nanocrystalline region. The electrochemical reaction for sodium-ion storage with vanadium-based MXenes can be derived from CV analysis (Fig. 9b), where the obvious sodiation and desodiation characteristics are evident from their reduction and oxidation peaks. Based on this, the reaction can be written as follows (eqn (6)),

$$\mathrm{VC} + x\mathrm{Na}^+ + x\mathrm{e}^- \leftrightarrow \mathrm{VNa}_x\mathrm{C} \tag{6}$$

At 0.1 mV s^{-1}, the capacitive contribution dominates, accounting for up to 48.1%, which is nearly half of the total contribution even at low scan rates (Fig. 9c). Except for the first cycle capacity loss, the developed material shows high stability and excellent rate capability (Fig. 9d), with a maximum of 111.2 mA h g^{-1} after 500 cycles even at a high current of 1 A g^{-1} (>89% capacity retention). This might be attributed to the interconnected 3D-ordered porous structures of VC particles embedded in the carbon layers, which bestowed long-term stability and better performance. Meanwhile, carbon layers provide well-ordered channels throughout the structure, facilitating the transfer of sodium ions. The structural robustness of the as-prepared VC@C electrode was further checked through various structural studies, such as grazing incidence X-ray diffraction (GXRD) and Raman spectra after post-cycling experiments. A slight blue shift during sodiation occurred, which might be due to the large size of the sodium ions. When a Na ion enters the system, it induces an irreversible tensile strain, which is also validated by the Raman spectra (Fig. 9h), where no peak shift was observed.

In another study, S. Kanade *et al.*[100] used reduced graphene oxide (rGO) to develop a multilayered sandwich-type VC@rGO nanocomposite as an anode material for SIBs, which shows outstanding electrochemical stability with 100% coulombic efficiency. Unlike a superficial carbon layer and active VC nanostructures, Wu *et al.*[98] developed vanadium carbide nanodots wrapped by N and P co-doped carbon nanosheets as anode materials for SIBs, as shown in Fig. 9e. The authors showed several advantages of the developed anode materials, such as high reversible capacity, superior rate capability, and capacity retention of 250 mA h g^{-1} at 0.1 A g^{-1}, 88 mA h g^{-1}, and 97%, respectively. A full cell was assembled using the developed anode and homemade NVP cathode (Fig. 9f), and its typical charge–discharge curve was compared with those of the corresponding half-cells. Interestingly, the *ex situ* XRD pattern at different voltages displayed a slight blue shift during sodiation, and it reverted to the original state during the desodiation process (Fig. 9g). VC with a ∼2–10 nm average diameter was prepared and homogeneously grown on N, P-doped carbon nanosheet scaffolds that shorten the Na-ion diffusion, resulting in excellent storage performance for SIBs. Recent reports also suggest that nanosized VC is essential to retain high ICE. The nanosized VC with a mean particle size of ∼40 nm can afford a reversible discharge capacity of 597.8 mA h g^{-1} at 0.1 Ag^{-1}.[29] In addition, MXenes, with their 2D structure, high electronic conductivity, high surface area, and flexibility, are well-known for their exciting characteristics with surface functional groups in the formulation $M_{n+1}X_nT_x$, wherein T represents the surface functional groups such as –OH, –O, and –F with $n = 1, 2, 3$. Considerable work was carried out with $n = 1, 2$.[24,26] However, K. Subramanyan *et al.* reported an interesting case of $V_4C_3T_x$ with $n = 3$ and electrochemical studies using ester and ether-based electrolytes ($V_4C_3T_x$-C and $V_4C_3T_x$-T) in both half- and full-cell configurations.[99] The step-by-step preparation procedure of $V_4C_3T_x$-C and $V_4C_3T_x$-T is shown in Fig. 9h. The presence of various elements and their atomic composition in the resultant structure was confirmed by EDAX and elemental mapping analysis, as demonstrated in Fig. 9i. The initial CV results concerning different scan rates indicated that the carbonate-based MXene shows better electrochemical properties than tetraglyme-based $V_4C_3T_x$-T, and their corresponding current contribution distribution plot is shown in Fig. 9j–l. Further, the cycling studies suggested that the carbonate-based half-cell shows an irreversible capacitance of 128 mA h g^{-1}, surpassing the tetraglyme-based half-cell. However, tetraglyme-based half-cells show higher retention than carbonate-based half-cells after 100 cycles. Similar rate retention properties exist in which $V_4C_3T_x$-T has higher rate capacitance at lower currents whereas, at higher current rates, properties exist in which $V_4C_3T_x$-T has higher rate capacitance at lower currents, whereas, at higher currents, $V_4C_3T_x$-T prevails. The authors further pointed out that the high-rate performance might be attributed to the disparity in the carbonate-based system, which has diffusion and capacitive-based Na-ion storage. The *in situ* impedance study revealed the formation of an SEI layer for $V_4C_3T_x$-C, whereas no such observations were made for $V_4C_3T_x$-T. These results substantiate electrolytes' effect on forming the SEI with the initial rise of coulombic efficiency, complicating the overall system. Concurrently, $V_4C_3T_x$ is also known to show higher thermodynamic and structural stability among the various MXenes. This facilitated their use as supports to enhance the cycling stability of conversion-type energy storage materials despite their low theoretical capacity. The electrochemical and cycling performances of various vanadium carbide-based anodes for SIBs are tabulated in Table 2.

Vanadium nitride (VN) combined with carbon fibers (VN@CF) was found to exhibit a maximum discharge capacity of

Table 2 Electrochemical and cycling performances of various niobium and vanadium carbide-based anodes for SIBs

Electrode material	Synthesis strategy	Electrolyte	Initial coulombic efficiency (%)	Cycling stability (mA h g^{-1})	Rate capability (mA h g^{-1})	Reference
VC@rGO	High-temperature carburization	1 M $LiPF_6$ in EC/DEC	94	523 (500 cycles)	—	100
		1 M $NaClO_4$ in EC/PC (1 : 1)	53	128 (500 cycles)	197 (100 cycles) @ 50 mA g^{-1}	
$(Co_{0.5}Ni_{0.5})S_2@V_4C_3T_x$	Pseudo-isotope synthesis	1 M $NaClO_4$ in EC/DC (1 : 1) with 5% FEC	54.5	1205 (100 cycles)	677.5 (1000 cycles) @ 0.1 A g^{-1}	101
VC-CNF@S	Melt-diffusion	0.2 M Na_2S_6	—	509 (80 cycles) @ 0.1C	379 (2000 cycles) @ 0.5C	102
$VMoS_2$	Hydrothermal method	1 M $NaSO_3CF_3$ in diglyme	89.9	548.1 (80 cycles)	207.4 (800 cycles) @ 20A g^{-1}	103
VN@CF	Molten-salt method	1 M $NaClO_4$ in EC/DC (1 : 1) with 5% FEC	34.49	88 (75 cycles) @ 0.1A g^{-1}	204 (500 cycles) @ 0.1 A g^{-1}	104
V_8C_7@CC	Hydrothermal method	1 M $NaPF_6$ in EC : DC (1 : 1)	99.8	203.9 (500 cycles) @ 0.1C	303 (500 cycles) @ 0.05C	105
α-VO_x/VC	Modified etching cum carburization process	2 M Na_2SO_4 0.004 M H_2SO_4		307 @ 50 mA g^{-1} (60 cycles)	96 @ 2000 mA g^{-1} (1800 cycles)	106

204 mA h g^{-1} at 0.1 A g^{-1} and to be stable for over 500 charge–discharge cycles, suggesting superior sodium storage performance.[104] The increased Na^+ storage behavior was due to pseudocapacitive redox processes at the electrode–electrolyte interface. As shown in Fig. 10a, VN@CF exhibits discrete redox peaks at 2.10 V and 0.74 V, which could be attributable to the surface faradaic reaction between sodium ions and VN during the sodiation/desodiation process. Furthermore, the overlapping of four CV curves demonstrates that the anode is structurally reversible as prepared. Interestingly, a solid irreversible cathodic peak at 0.51 V was discovered during the first discharge cycle, indicating electrolyte breakdown and creating a solid electrolyte interface (SEI). A strong cathodic peak at 0.01 V indicates that sodium ions have been inserted into the carbon matrix. As shown in Fig. 10b, the V@CF anode has excellent rate performance for sodium storage, with a mean reversible discharge capacity ranging from 159.2 mA h g^{-1} to 88 mA h g^{-1} at C-rates of 0.1 to 1 A g^{-1}. The production of the SEI during the initial discharge cycle results in a low coulombic efficiency of 34.49% for VN@CF. The enhanced electrolyte wettability and consistent activation of the VN@CF electrode may have contributed to the nearly 100% increase in coulombic efficiency in subsequent cycles. The first charge–discharge plot revealed a linear *I–V* trend, indicating the pseudocapacitive mechanism for storing sodium ions, as illustrated in Fig. 10c. Many discharge curves were recorded below 0.8 V, verifying the anode material's properties. The as-made VN@CF's remarkable cycling performance is further proven by its ability to maintain a reversible capacity of 204 mA h g^{-1} at 0.1 A g^{-1}, even after 500 cycles, as shown in Fig. 10d. The electrical conductivity of VN@CF is examined by impedance spectroscopy (Fig. 10e), which shows the lowest charge transfer resistance of 139.6 Ω after 500 cycles compared to its initial value (187.4 Ω). Additionally, the high discharge capacity of 132.6 mA h g^{-1}, even after 6600 cycles at 1 A g^{-1}, confirms the robust cycling stability of VN@CF (Fig. 10f). Because of this structural variability, VN@CF hybrid structures have demonstrated advantageous properties that improve the overall coulombic efficiency of next-generation SIBs.

4.2. Electrochemical behaviors of vanadium carbide/metal sulfide composites

This section deals with the electrochemical properties of vanadium carbide and its composite-based MXenes. Y. Li *et al.*[101] designed a unique $(Co_{0.5}Ni_{0.5})S_2@V_4C_3T_x$ conversion type electrode with carbon-embedded $C@NCS@V_4C_3T_x$ as an anode material for SIBs. The $V_4C_3T_x$ in the electrodes can improve the interfacial stability and electronic conductivity of consecutive sodium charge–discharge cycles. The carbon layer can act as a conductive support to enhance the robustness of the anode counterpart for SIBs. The authors interestingly claim that the step-by-step assembly strategy developed $C@NCS@\ V_4C_3T_x$ resembles the human skeleton ($V_4C_3T_x$), muscle (active substance $(Co_{0.5}Ni_{0.5})S_2$, NCS), and skin (PDA-carbon layer, C). The structural changes during the sodiation and de-sedation process of the SIB cell using these electrodes are

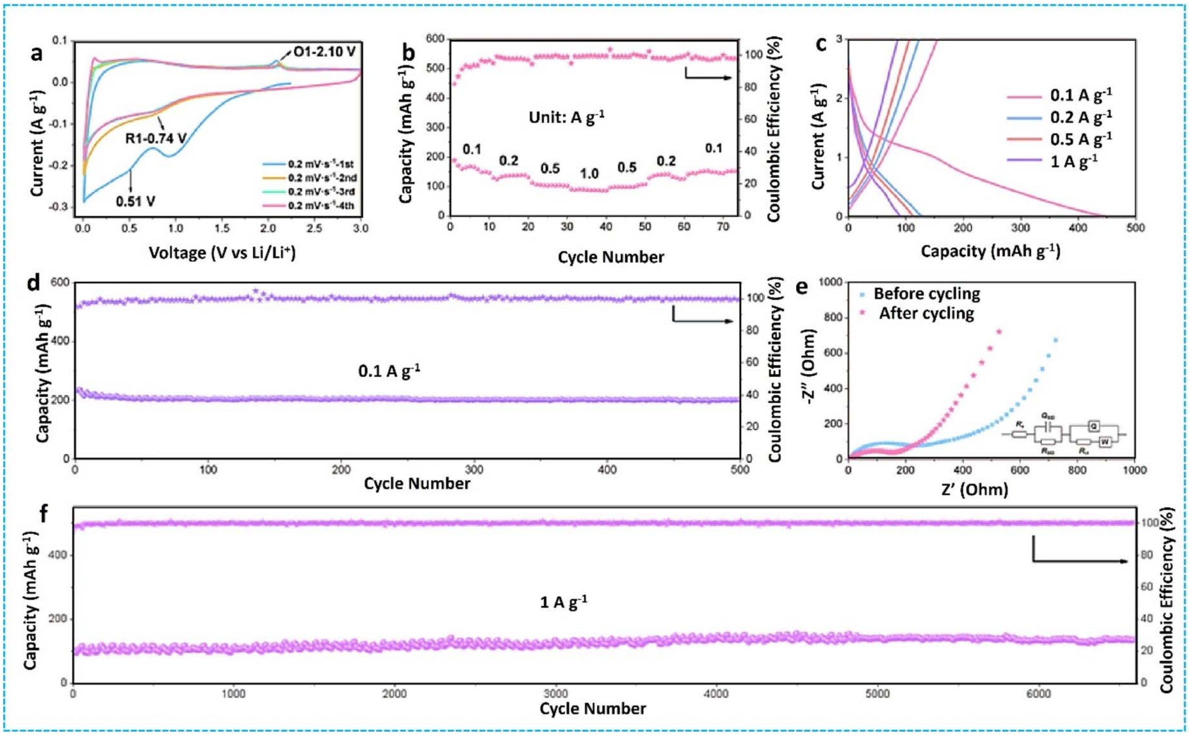

Fig. 10 Sodium storage characteristics of the VN@CF electrode: (a) CV curve at a sweep rate of 0.2 mV s^{-1}, (b) rate capability plot, (c) initial GCD profile at voltages between 0.1 and 1 A g^{-1}, (d) cycling behavior at a C-rate of 0.1 A g^{-1}, (e) impedance curve for the device before and after testing, and (f) cycling behavior at a C-rate of 1 A g^{-1}, reproduced with permission from ref. 104, Copyright 2023, Elsevier.

schematically presented in Fig. 11a. Their corresponding SEM images in the inset of Fig. 11a indicate that there are no significant changes in the electrode structure before and after testing. This multi-component C@NCS@ $V_4C_3T_x$ hybrid has exhibited an ultrahigh reversible specific capacity of 705.6 mA h g^{-1} at 0.1 A g^{-1}. The synergistic combination has facilitated overcoming the disadvantages, including instability associated with the electrode, volume expansion during Na^+ insertion/de-insertion cycles, and loss of cycling stability while improving the charge transfer and ion diffusion. The authors further checked the commerciality of the full-cell configuration using an NVP cathode, which is linked with the stop-watch device, as shown in Fig. 11b–d, to identify the practicability of the employed cell. The electrochemical properties such as CV, GCD, EIS, and capacity retention of the full SIB cell using the proposed electrodes are displayed in Fig. 11e–i. A high reversible capacity of 399.4 mA h g^{-1} was reported with a cell voltage of 2.5–4 V at 0.1 A g^{-1} over 100 cycles. Further, the rate capability of the full-cell was identified by analyzing the cycling performance at different C-rates, maintaining a high capacity of 423.6 mA h g^{-1} even at a high C-rate of 5.0 A g^{-1}. These observations confirm the potential viability of C@NCS@ $V_4C_3T_x$ anodes in high-performance SIBs.

Liu *et al.* developed S-vacancy enriched MoS_2@C anchored on V_2C-MXene to improve stability in conversion-type materials, achieving 337.3 mA h g^{-1} at 1 A g^{-1} for sodium-ion batteries (SIBs).[107] Their *in situ* carbonization method facilitated the layering of MoS_2 nanosheets on conductive V_2C-MXene, creating S vacancies and enhancing charge distribution. This synergistic property boosts electronic conductivity and accelerates ion diffusion, addressing challenges like poor conductivity and slow redox reactions in MoS_2 anodes, which are otherwise promising due to their layered structure. The vanadium-combined MoS_2 (VMS_2) framework, synthesized *via* a one-pot hydrothermal method, exhibited initial charge and discharge capacities of 521.5 and 580.1 mA h g^{-1} with a coulombic efficiency of 89.9% in the range of 0.3–3.0 V (Fig. 12a and b). A stable SEI layer, formed with the ether electrolyte, facilitated sodium ion migration, leading to improved cycling stability of the VM-43 sample, demonstrated the highest specific capacity of 455.6 mA h g^{-1} and maintained over 100% coulombic efficiency after 260 cycles and high capacity retention even at 20 A g^{-1} (Fig. 12c–e), confirming its superior electrochemical performance compared to other MoS_2-based anodes (Fig. 12f). Theoretical results further indicate that vanadium reduces the energy barrier for sodium ion migration and enhances electronic conductivity, while VMS_2's disordered features provide ample active sites for sodium ion storage.

4.3. Electrochemical behaviors of heterojunction-based vanadium carbide anodes

Unlike MoS_2, a double vanadium-based heterojunction comprising sulfide and carbide was constructed by Chen *et al.*[108] The vanadium bridging the S and V (S–V–C) enhanced the 3D channel of electrons for efficient ion diffusion and electron/charge transport. The VS_4–V_2CT_x composite showed an excellent discharge capacity of 322 mA h g^{-1} at 10 A g^{-1} even after

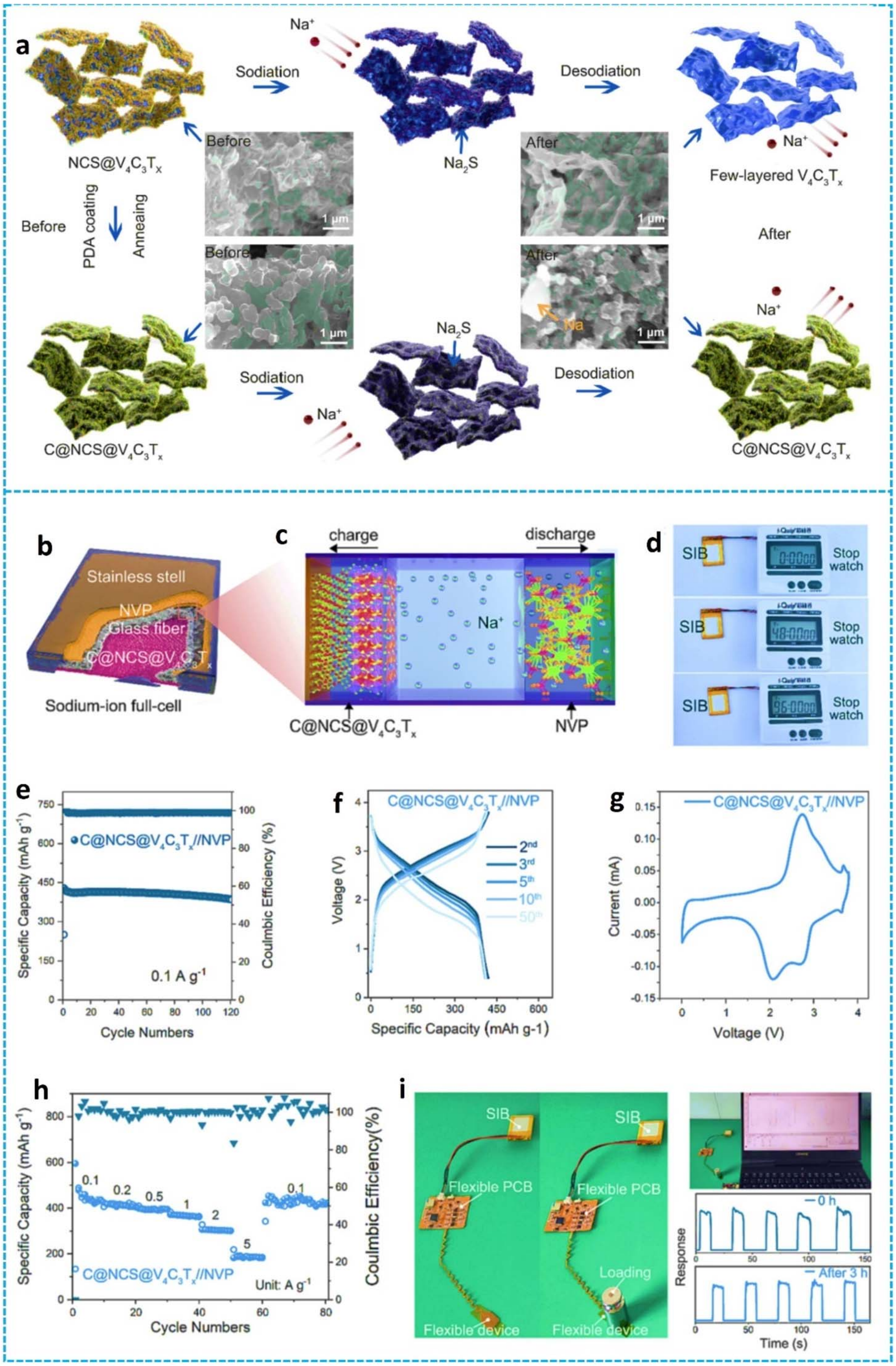

Fig. 11 (a) Representation of the structural characteristics and FE-SEM micrographs of C@NCS@$V_4C_3T_x$ and NCS@$V_4C_3T_x$ hybrid electrodes before and after the cycling tests, (b–i) electrochemical performance of the C@NCS@$V_4C_3T_x$//NVP SIB, including (b and c) schematic diagram of the SIB full cell comprising C@NCS@$V_4C_3T_x$ and NVP electrodes, (d) optical photo image of the fully powered SIB cell, (e) cycling behavior of the C@NCS@$V_4C_3T_x$//NVP full cell, (f) GCD profile of C@NCS@$V_4C_3T_x$//NVP, (g) their corresponding cyclic voltammetry curve, (h) rate capability of the SIB full cell, (i) flexible integrated device constructed with a SIB pouch cell which is charged for 3 h at the working voltage of 1 V, reproduced with permission from ref. 101, Copyright 2023, Elsevier.

4000 cycles. Multi-electron reactions associated with numerous valence states have promoted the applicability of VS_2 as a potential material for SIBs with a redox reaction ($8Na^+ + VS_4 + 8e^- \rightarrow V + 4Na_2S$) with a theoretical capacity of 1196 mA h g^{-1}. Nevertheless, due to rapid charge–discharge reactions, the decay in electrochemical performance associated with phase transformation is inevitable for VS_2. Unlike the usual utilization of the carbon matrix to suppress the crystal phase transformation of the active material, the authors used a polar matrix of V_2CT_x and VS_4-V_2CT_x composites constructed *via*

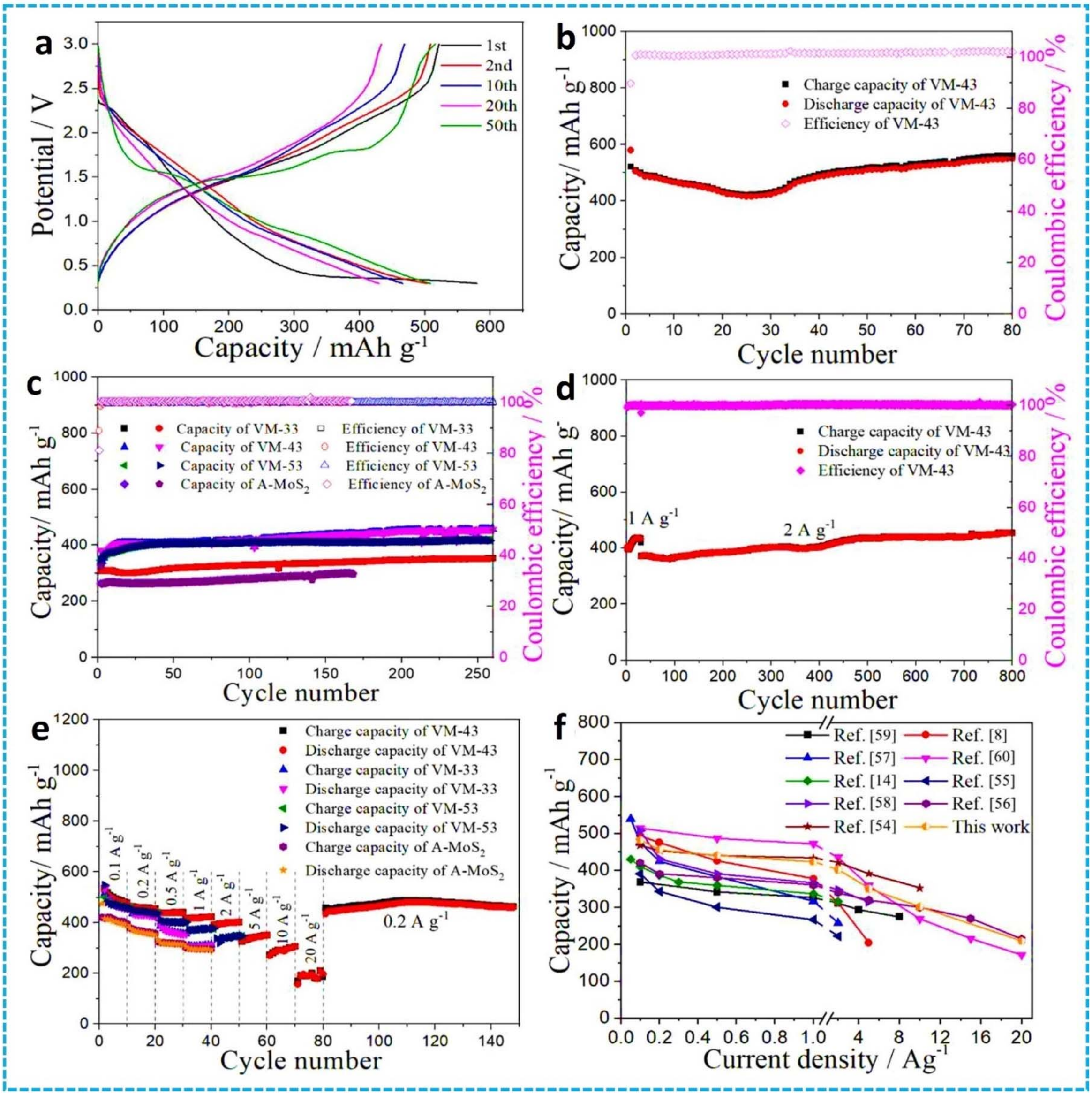

Fig. 12 (a) Typical GCD profile of the VM-43 based anode in the 1st, 2nd, 10th, 20th, and 50th cycles at 100 mA g^{-1}, electrochemical cycling characteristics of VM-43 anodes at various C-rates: (b) 100 mA g^{-1} and (c) 2 A g^{-1}, (d) cycling behavior at a constant C-rate of 1 A g^{-1} for VM-33, 43, and 53 anodes, and (e and f) their corresponding rate capability curve and their comparison with other MoS_2 based anodes, reproduced with permission from ref. 103, Copyright 2021, Elsevier.

solvothermal synthesis. Despite all these efforts to elevate the performance of anode materials for SIBs, the role of the C–C matrix is highly recognized. Even among all MXenes, carbides have gained much attention, possibly due to the impending role played by the C matrix. These results suggest that more insights could be drawn from observing graphene or carbon-based materials as anodes to develop the next generation of anode materials using new transition metal carbides. Nam *et al.* reported that V_8C_7 nanowires are axially decorated over carbon cloth and can be used as potential anodes for SIBs.[105] The V_8C_7 NWs grown on carbon cloth developed *via* reduction in the presence of carbon sources have yielded 176.34 mA h g^{-1} capacity at 0.1C with improved cycling stability for 300 cycles. Using carbon cloth as a current collector, the approach provides a reservoir for active sites to store the cations. Meanwhile, advantageous features such as a high surface area (183.27 m^2 g^{-1}) and one-dimensional nanowire growth of the active material efficiently limited the volume expansion during the GCD process, achieving high stability. Due to the combination of carbon cloth and active V_8C_7, a dual ion accepting phenomenon occurred, improving the Na ion mass transport and rate performance. Conversely, metal ion intercalation (Mn^{2+}) was adopted to enhance cycling stability by limiting volume expansion during Na^+ insertion and de-insertion. The metal ion intercalation is expected to form a V–O–Mn covalent bond, stabilizing the active material and inhibiting structural collapse.[109] A similar strategy has been used for sodium–sulfur (Na–S) batteries, wherein vanadium carbide nanoparticles were incorporated into the carbon nanofibers to accelerate the redox reactions. Later, Zhang *et al.*[106] studied the effect of surface amorphous vanadium oxide conformally decorated over layered V_2C MXene (a-VO_x/V_2C) to boost sodium insertion and de-insertion reversibility. The amorphous outer layer of VO_x provides enough vacancies and open pathways, while the active V_2C provides abundant electron/ion transfer channels, which boost coulombic efficiency.[106] The anodic-oxidation-formed heterostructure a-VO_x/V_2C exhibits a high reversible capacity of 307 mA h g^{-1} at 50 mA g^{-1} and considerable cycling stability as a cathode for SIBs. Interestingly, *in situ* Raman and TEM results revealed that the valence oxidation between V^{4+} and V^{5+} in the disordered framework facilitates a fast ion diffusion pathway for improved coulombic efficiency, highlighting the necessity of the VO_x layer and stabilizer.

Additionally, the sodium-ion storage performance of V_2C MXenes was studied as a cathode for sodium-ion hybrid capacitors against a hard carbon anode.[110] The V_2C MXenes were prepared by a selective etching process, in which the V_2C works in the potential range between 1.0 and 3.5 V in the cathode region, which delivered a maximum of 100 F g^{-1} at 0.2 mV s^{-1}. The full cell delivered a maximum cell voltage of 3.5 V with a specific capacity of 50 mA h g^{-1}. XRD peaks at various voltages indicated several interlayer gaps within the lattice unit, with an expansion and shrinkage of 2.3 Å occurring during the sodiation and desodiation processes. It was observed that the presence of the V_2AlC MAX phase in the electrode resulted from an incomplete chemical reaction during synthesis. This MAX phase was electrochemically inactive, as evidenced by a stagnant peak at 13° during both the sodiation and desodiation processes.

5. Summary, outlook, and future perspectives

This review elaborates on niobium- and vanadium carbide-based MXenes as potential anodes for improved Na-storage performance in SIBs. Since various articles have described the synthesis and structural features of these MXenes, the review focuses on the electrochemical storage properties of Nb and V-based MXenes. In contrast to the understanding of the chemistry of two-dimensional (2D) metal carbides, especially niobium and vanadium carbides (Nb/V–Cs), there is limited research on these materials as electrode materials for SIBs. Nb/V–Cs are an emerging class of 2D materials gaining much interest due to high metallic-like conductivity, stability, functionalization ability with surface O, F, and OH groups, and enrichment with defects for improved electrochemical performance. However, much attention has been paid to understanding and improving the anodic behavior of Nb/V–Cs in SIBs. Yet, recent progress highlights the need for further insights to improve the electrochemical properties of Nb/V–Cs. On another note, carbon remains the main component, along with the active phase, to enhance the electrochemical behaviors of these carbides. However, unlike LIBs, there have been limited reports on considering different forms of carbon (nanofibers, sheets, and 3D structures) to host Na^+ ions.

Furthermore, it highlights the feasibility of employing these Nb–C/VC-based anodes to achieve high initial coulombic efficiency and rate capabilities for SIB applications. Specifically, Nb–C and VC are promising anode materials for SIBs due to their high electrical conductivity, thermal stability, high cycling life, and relatively large theoretical capacity. Since these elements are abundant in the Earth's crust, they reduce the capital cost of the proposed electrode materials for the preparation process. Owing to these advantageous properties, these materials offer superior power performance, cycle life, and energy and power densities. In addition, the strong carbide bonds in niobium and vanadium carbides facilitate hosting a more significant number of sodium ions, enhancing the coulombic efficiency and reversible capacity. VC has a higher theoretical capacity (~300 mA h g^{-1}) and offers excellent electrical conductivity, making it suitable for applications that require high energy density and power performance. In contrast, Nb–C provides better structural stability during volume changes and enhances cycling and long-term performance by forming a more stable SEI. VC may be more appropriate for high capacity and fast charging applications, while Nb–C may be better suited for applications that demand stable performance over extended cycles. Consequently, Nb–C is generally regarded as more stable and capable of ensuring consistent performance over time compared to VC, which primarily focuses on high-capacity requirements.

However, several challenges that restrict them in potential SIB applications are listed as follows: (a) the potential toxicity of vanadium raises concerns about sustainability and environmental impacts during product manufacturing and recycling, (b) these electrodes need to accommodate the large size of sodium ions, which leads to sluggish sodium ion diffusion, (c) they offer very low initial coulombic efficiency because of the irreversible reactions including the formation of a SEI and electrolyte deterioration, (d) the overall efficiency of the cell can be hindered by the continuous formation of a SEI layer, which consumes a large number of sodium ions, and (e) large mass loading of these electrodes may affect the overall energy density of the battery. The researchers propose that these electrodes can accommodate more sodium ions, leading to the sluggish kinetics of sodium ions and limiting the cell's overall coulombic efficiency. Henceforth, future studies will focus more on the morphology and microstructure of these carbide materials to improve overall sodium ion diffusion and battery performance. To mitigate these shortcomings, surface engineering modification processes such as doping or coating with conductive materials can improve the initial coulombic efficiency and stabilize the anode-electrolyte interface, reducing SEI-related complications. Hence, introducing transition metal sulfides, oxides, and 2D MOFs into the MXene matrix improves surface wettability, redox kinetics, active charge sites, electronic conductivity, surface area, coulombic efficiency, and SIB reversibility. The electrochemical flexibility and overall performance of these composite MXenes are always superior to those of their pure counterparts. Furthermore, there are many possibilities to improve the coulombic efficiency of Nb/V–Cs using approaches such as developing composite materials using metal oxides/sulfides/phosphides, as little has been understood so far. These composite anodes provide significant potential for increasing the long-term durability and cycling performance of these SIBs.

In addition, to improve the rate capability and capacity retention of SIBs, Nb–C or VC can be incorporated into other plausible materials to construct hybrid anode designs that improve electrochemical performance. Future advancements in scalable and cost-effective synthesis techniques will be essential for commercializing these materials. Furthermore, realizing the distinct reaction pathways and sodium storage processes in carbide-based anodes will provide more insights for the development of future SIBs. Recent advancements suggest that Nb–C and VC anodes have the potential to enhance the performance of SIBs, positioning them as competitive alternatives to lithium-ion batteries, particularly in large-scale energy storage applications. This is attributed to factors such as cost advantages and resource accessibility. Defect engineering could also be a viable strategy as it can enable reversible and fast ion intercalation–deintercalation owing to the defects acting as open pathways for ion migration. On the other hand, considering that the stability of the SEI layer contributes significantly to reversibility, such approaches need to be carried out to develop the next generation of materials. Due to the abundance of sodium sources, attention to SIBs could change the economic dimensions of energy storage systems, and materials such as Nb–C/VC could offer high sustainability to such approaches. By considering the recent advancements, Nb–C/VC composites have the potential to improve SIB performance significantly and become commercially viable owing to their high specific capacities, extended cycle life, and superior rate capability.

Finally, based on our views, we conclude that the research into advanced sodium-ion anodes should focus on microstructure optimization and surface modification techniques, such as doping, compositing, integrating conversion, alloying, and insertion-based materials with other conductive materials, to enhance sodium ion diffusion and stabilize the SEI layer. Given niobium and vanadium's abundance and relative cost-effectiveness, these materials could be sustainable alternatives to LIBs, particularly for grid-scale energy storage. However, further investigation into defect engineering, hybrid anode design, and scalable synthesis processes is required to advance the commercialization of Nb–C and VC-based SIBs. In addition, enhanced synthesis strategies and molecular-level interface engineering and understanding would be able to address current challenges related to scalability, stability, and cost reduction. Overall, Nb/V–C electrodes can potentially have a vital impact on achieving widespread usage of large-scale SIB applications.

Data availability

No primary research results, software or code have been included and no new data were generated or analysed as part of this review.

Author contributions

K. Karuppasamy: conceptualization, methodology and writing – original draft. Ganesh Kumar Veerasubramani: writing – original draft, software, and review and editing. Vishwanath Hiremath: resources and writing the original draft. Dhanasekaran Vikraman: writing – original draft. P. Santhoshkumar: review and editing. Georgios N. Karanikolos: visualization and supervision. Ali Abdulkareem Alhammadi: visualization, supervision, and validation. Hyun-Seok Kim: validation and review and editing. Akram Alfantazi: conceptualization, visualization, and writing – original draft.

Conflicts of interest

The authors declare no conflicts of interest.

Acknowledgements

One of the authors, Dr K. K., gratefully acknowledges the Khalifa University of Science and Technology, Abu Dhabi, for financial support. Dr G. K. V. likewise gratefully acknowledges Khalifa University for funding this work through the CIRA project (8474000424) with the support of the Center for Catalysis and Separations (CeCaS, Award No. RC2-2018-024).

References

1 T. Perveen, M. Siddiq, N. Shahzad, R. Ihsan, A. Ahmad and M. I. Shahzad, *Renewable Sustainable Energy Rev.*, 2020, **119**, 109549.

2 P. Santhoshkumar, K. Karuppasamy, D. Vikraman, T. Maiyalagan and H.-S. Kim, *Surf. Interfaces*, 2023, **41**, 103175.

3 T. Yang, S. Yun, C. Wang, Y. Zhang, J. Dang, G. Yang, Z. Gao, D. Qiao and M. Zhang, *J. Mater. Sci. Technol.*, 2023, **37**, 101371.

4 E. A. Zhurakovskii, in *Refractory Carbides*, ed. G. V. Samsonov, Springer US, New York, NY, 1974, pp. 187–200, DOI: 10.1007/978-1-4684-8598-1_21.

5 K. M. Abraham, *ACS Energy Lett.*, 2020, **5**, 3544–3547.

6 H. Chang, X. Liu, S. Zhao, Z. Liu, R. Lv, Q. Zhang and T.-F. Yi, *Adv. Funct. Mater.*, 2024, **34**, 2313491.

7 K. Karuppasamy, D. Vikraman, S. Hussain, B. Thirumalraj, P. Santhoshkumar, H. Parangusan, H.-C. Park, J. Jung and H.-S. Kim, *J. Energy Chem.*, 2023, **79**, 569–580.

8 C. Yang, S. Xin, L. Mai and Y. You, *Adv. Energy Mater.*, 2021, **11**, 2000974.

9 D. Yang, J. Li, C. Liu, W. Xing and J. Zhu, *J. Energy Chem.*, 2023, **82**, 122–138.

10 D. Vikraman, S. Hussain, Z. Abbas, K. Karuppasamy, W.-S. Kang, P. Santhoshkumar, A. Kathalingam, J. Jung and H.-S. Kim, *J. Mater. Sci. Technol.*, 2023, **162**, 44–56.

11 P. Santhoshkumar, T. Subburaj, Y. Lee, K. Karuppasamy, D. Vikraman and H.-S. Kim, *J. Energy Storage*, 2023, **69**, 107915.

12 K. Karuppasamy, D. Vikraman, J.-H. Choi, R. Bose, A. Nichelson, T. Maiyalagan and H.-S. Kim, *J. Mater. Res. Technol.*, 2020, **9**, 5216–5227.

13 B. Huang, H. Wang, S. Liang, H. Qin, Y. Li, Z. Luo, C. Zhao, L. Xie and L. Chen, *Energy Storage Mater.*, 2020, **32**, 105–114.

14 C. Huang, Y. Liu, J. Li, Z. Miao, X. Cai, Z. Wu, H. Yu, L. Yan, L. Zhang and J. Shu, *J. Mater. Sci. Technol.*, 2023, **140**, 135–141.
15 X. Yang and A. L. Rogach, *Adv. Energy Mater.*, 2020, **10**, 2000288.
16 H. S. Hirsh, Y. Li, D. H. S. Tan, M. Zhang, E. Zhao and Y. S. Meng, *Adv. Energy Mater.*, 2020, **10**, 2001274.
17 Y.-Y. Xiao, Y.-H. Liu, B.-B. Liu, Z.-G. Qi, Y.-B. Zhang, F.-S. Liu and G.-H. Qin, *Rare Met.*, 2023, **42**, 4048–4059.
18 J. Peng, W. Zhang, Q. Liu, J. Wang, S. Chou, H. Liu and S. Dou, *Adv. Mater.*, 2022, **34**, 2108384.
19 D. Hou, D. Xia, E. Gabriel, J. A. Russell, K. Graff, Y. Ren, C.-J. Sun, F. Lin, Y. Liu and H. Xiong, *ACS Energy Lett.*, 2021, **6**, 4023–4054.
20 Q. Liu, R. Xu, D. Mu, G. Tan, H. Gao, N. Li, R. Chen and F. Wu, *Carbon Energy*, 2022, **4**, 458–479.
21 Y. Chu, J. Zhang, Y. Zhang, Q. Li, Y. Jia, X. Dong, J. Xiao, Y. Tao and Q.-H. Yang, *Adv. Mater.*, 2023, **35**, 2212186.
22 M. K. Aslam, T. S. AlGarni, M. S. Javed, S. S. A. Shah, S. Hussain and M. Xu, *J. Energy Storage*, 2021, **37**, 102478.
23 M. K. Aslam and M. Xu, *Nanoscale*, 2020, **12**, 15993–16007.
24 P. Ma, D. Fang, Y. Liu, Y. Shang, Y. Shi and H. Y. Yang, *Adv. Sci.*, 2021, **8**, 2003185.
25 K. Liang, A. Tabassum, A. Majed, C. Dun, F. Yang, J. Guo, K. Prenger, J. J. Urban and M. Naguib, *InfoMat*, 2021, **3**, 1422–1430.
26 P. Cai, Q. He, L. Wang, X. Liu, J. Yin, Y. Liu, Y. Huang and Z. Huang, *Ceram. Int.*, 2019, **45**, 5761–5767.
27 L. Du, H. Duan, Q. Xia, C. Jiang, Y. Yan and S. Wu, *ChemistrySelect*, 2020, **5**, 1186–1192.
28 C. Lamiel, I. Hussain, J. H. Warner and K. Zhang, *Mater. Today*, 2023, **63**, 313–338.
29 R. J. Liu, L. X. Yang, J. T. Wu, H. P. Bu, H. J. Liu, C. L. Zeng and C. Fu, *Electrochim. Acta*, 2022, **403**, 139674.
30 S. A. Zahra, B. Anasori, M. Z. Iqbal, F. Ravaux, M. Al Tarawneh and S. Rizwan, *APL Mater.*, 2022, **10**, 060901.
31 Q. Shan, X. Mu, M. Alhabeb, C. E. Shuck, D. Pang, X. Zhao, X.-F. Chu, Y. Wei, F. Du, G. Chen, Y. Gogotsi, Y. Gao and Y. Dall'Agnese, *Electrochem. Commun.*, 2018, **96**, 103–107.
32 P. A. Rasheed, R. P. Pandey, F. Banat and S. W. Hasan, *Matter*, 2022, **5**, 546–572.
33 M. Naguib, J. Halim, J. Lu, K. M. Cook, L. Hultman, Y. Gogotsi and M. W. Barsoum, *J. Am. Chem. Soc.*, 2013, **135**, 15966–15969.
34 Y. Wang, J. Shen, L.-C. Xu, Z. Yang, R. Li, R. Liu and X. Li, *Phys. Chem. Chem. Phys.*, 2019, **21**, 18559–18568.
35 Y. Chen, Y. Huang, Q. Xu, L. Yang, N. Jiang and S. Yin, *Mater. Horiz.*, 2024, DOI: 10.1039/D4MH00674G.
36 Q. Wang, J. Xu, W. Zhang, M. Mao, Z. Wei, L. Wang, C. Cui, Y. Zhu and J. Ma, *J. Mater. Chem. A*, 2018, **6**, 8815–8838.
37 N. Thatsami, P. Tangpakonsab, P. Moontragoon, R. Umer, T. Hussain and T. Kaewmaraya, *Phys. Chem. Chem. Phys.*, 2022, **24**, 4187–4195.
38 S. Liu, F. Hu, W. Shao, W. Zhang, T. Zhang, C. Song, M. Yao, H. Huang and X. Jian, *Nano-Micro Lett.*, 2020, **12**, 135.
39 W. Bi, S. Li, W. Wang, Y. Liu, J. Shen, G. Gao, Z. Zhang, G. Wu and G. Cao, *Energy Storage Mater.*, 2024, **71**, 103568.
40 M. Naguib, M. Kurtoglu, V. Presser, J. Lu, J. Niu, M. Heon, L. Hultman, Y. Gogotsi and M. W. Barsoum, *Adv. Mater.*, 2011, **23**, 4248–4253.
41 M. Naguib, J. Come, B. Dyatkin, V. Presser, P.-L. Taberna, P. Simon, M. W. Barsoum and Y. Gogotsi, *Electrochem. Commun.*, 2012, **16**, 61–64.
42 M. R. Lukatskaya, O. Mashtalir, C. E. Ren, Y. Dall'Agnese, P. Rozier, P. L. Taberna, M. Naguib, P. Simon, M. W. Barsoum and Y. Gogotsi, *Science*, 2013, **341**, 1502–1505.
43 Y. Xie, Y. Dall'Agnese, M. Naguib, Y. Gogotsi, M. W. Barsoum, H. L. Zhuang and P. R. C. Kent, *ACS Nano*, 2014, **8**, 9606–9615.
44 X. Liang, A. Garsuch and L. F. Nazar, *Angew. Chem. Int. Ed.*, 2015, **54**, 3907–3911.
45 T. Y. Ma, J. L. Cao, M. Jaroniec and S. Z. Qiao, *Angew. Chem. Int. Ed.*, 2016, **55**, 1138–1142.
46 B. Li, D. Zhang, Y. Liu, Y. Yu, S. Li and S. Yang, *Nano Energy*, 2017, **39**, 654–661.
47 Z. Wang, X. Chen, F. Shen, X. Hang and C. Niu, *Adv. Theory Simul.*, 2018, **1**, 1800059.
48 J. Luo, C. Wang, H. Wang, X. Hu, E. Matios, X. Lu, W. Zhang, X. Tao and W. Li, *Adv. Funct. Mater.*, 2019, **29**, 1805946.
49 Y. Tian, Y. An, C. Wei, B. Xi, S. Xiong, J. Feng and Y. Qian, *ACS Nano*, 2019, **13**, 11676–11685.
50 M. Naguib, O. Mashtalir, J. Carle, V. Presser, J. Lu, L. Hultman, Y. Gogotsi and M. W. Barsoum, *ACS Nano*, 2012, **6**, 1322–1331.
51 K. R. G. Lim, M. Shekhirev, B. C. Wyatt, B. Anasori, Y. Gogotsi and Z. W. Seh, *Nat. Synth.*, 2022, **1**, 601–614.
52 X. Li, Z. Huang, C. E. Shuck, G. Liang, Y. Gogotsi and C. Zhi, *Nat. Rev. Chem*, 2022, **6**, 389–404.
53 J. Chen, Q. Huang, H. Huang, L. Mao, M. Liu, X. Zhang and Y. Wei, *Nanoscale*, 2020, **12**, 3574–3592.
54 M. Khazaei, A. Mishra, N. S. Venkataramanan, A. K. Singh and S. Yunoki, *Curr. Opin. Solid State Mater. Sci.*, 2019, **23**, 164–178.
55 G. Murali, J. K. Reddy Modigunta, Y. H. Park, J.-H. Lee, J. Rawal, S.-Y. Lee, I. In and S.-J. Park, *ACS Nano*, 2022, **16**, 13370–13429.
56 Q. Jiang, Y. Lei, H. Liang, K. Xi, C. Xia and H. N. Alshareef, *Energy Storage Mater.*, 2020, **27**, 78–95.
57 J. A. Kumar, P. Prakash, T. Krithiga, D. J. Amarnath, J. Premkumar, N. Rajamohan, Y. Vasseghian, P. Saravanan and M. Rajasimman, *Chemosphere*, 2022, **286**, 131607.
58 X. Zhan, C. Si, J. Zhou and Z. Sun, *Nanoscale Horiz.*, 2020, **5**, 235–258.
59 B. R. Anne, J. Kundu, M. K. Kabiraz, J. Kim, D. Cho and S.-I. Choi, *Adv. Funct. Mater.*, 2023, **33**, 2306100.
60 P. Eghbali, A. Hassani, S. Wacławek, K.-Y. Andrew Lin, Z. Sayyar and F. Ghanbari, *Chem. Eng. J.*, 2024, **480**, 147920.
61 S. Ravuri, P. S. Wrobel, S. Gorantla, C. Bazioti, M. F. Sunding, K. Lis, R. Jedrzejewski, S. Sartori, S. Diplas, A. E. Gunnæs and A. Bachmatiuk, *Nanotechnology*, 2024, **35**, 155601.

62 T. Zhang, L. Pan, H. Tang, F. Du, Y. Guo, T. Qiu and J. Yang, *J. Alloys Compd.*, 2017, **695**, 818–826.

63 X. Zhu, K. Yang, Z. Zhang, S. He, Z. Shen, W. Jiang, Y. Huang, Y. Xu, Q. Jiang, L. Pan, Q. Li and J. Yang, *ACS Appl. Mater. Interfaces*, 2024, **16**, 28709–28718.

64 L. Liu, M. Orbay, S. Luo, S. Duluard, H. Shao, J. Harmel, P. Rozier, P.-L. Taberna and P. Simon, *ACS Nano*, 2022, **16**, 111–118.

65 Y. Ou, P. Zhang, R. A. Soomro, N. Qiao, H. Cui and B. Xu, *Inorg. Chem. Front.*, 2024, **11**, 1423–1433.

66 S. Siddique, A. Waheed, M. Iftikhar, M. T. Mehran, M. Z. Zarif, H. A. Arafat, S. Hussain and F. Shahzad, *Prog. Mater. Sci.*, 2023, **139**, 101183.

67 Y. Wei, P. Zhang, R. A. Soomro, Q. Zhu and B. Xu, *Adv. Mater.*, 2021, **33**, 2103148.

68 X.-H. Zha, Q. Huang, J. He, H. He, J. Zhai, J. S. Francisco and S. Du, *Sci. Rep.*, 2016, **6**, 27971.

69 B. Fu, J. Sun, C. Wang, C. Shang, L. Xu, J. Li and H. Zhang, *Small*, 2021, **17**, 2006054.

70 X. Jiang, A. V. Kuklin, A. Baev, Y. Ge, H. Ågren, H. Zhang and P. N. Prasad, *Phys. Rep.*, 2020, **848**, 1–58.

71 M. P. Bilibana, *Adv. Sens. Energy Mater.*, 2023, **2**, 100080.

72 R. B. Rakhi, B. Ahmed, M. N. Hedhili, D. H. Anjum and H. N. Alshareef, *Chem. Mater.*, 2015, **27**, 5314–5323.

73 X. Li, C. Wang, Y. Cao and G. Wang, *Chem.–Asian J.*, 2018, **13**, 2742–2757.

74 J. F. Smith, O. N. Carlson, R. R. De Avillez and J. Nuclear, *Mater*, 1987, **148**, 1–16.

75 P. Barnes, Y. Zuo, K. Dixon, D. Hou, S. Lee, Z. Ma, J. G. Connell, H. Zhou, C. Deng, K. Smith, E. Gabriel, Y. Liu, O. O. Maryon, P. H. Davis, H. Zhu, Y. Du, J. Qi, Z. Zhu, C. Chen, Z. Zhu, Y. Zhou, P. J. Simmonds, A. E. Briggs, D. Schwartz, S. P. Ong and H. Xiong, *Nat. Mater.*, 2022, **21**, 795–803.

76 D. Dai, S. Roszak and K. Balasubramanian, *J. Phys. Chem. A*, 2000, **104**, 9760–9769.

77 M. W. Barsoum, *Prog. Solid State Chem.*, 2000, **28**, 201–281.

78 T. Tsuchida and Y. Azuma, *J. Mater. Chem.*, 1997, **7**, 2265–2268.

79 B. Vishwanadh, T. S. R. C. Murthy, A. Arya, R. Tewari and G. K. Dey, *J. Alloys Compd.*, 2016, **671**, 424–434.

80 J. Hu, B. Xu, C. Ouyang, Y. Zhang and S. A. Yang, *RSC Adv.*, 2016, **6**, 27467–27474.

81 S. Wang, L. Shao, L. Yu, J. Guan, X. Shi, Z. Sun, J. Cai, H. Huang and A. Trukhanov, *Energy Technol.*, 2021, **9**, 2100298.

82 M. Liu, D. Zhang, B. Liu, C. Tian, B. Zhao, Y. Wang, Y. Wang, Y. Hu, L. Kong, D. Luo and Z. Chen, *Nano Energy*, 2022, **103**, 107795.

83 Y. Wang, J. Li, P. Song, J. Yang, Z. Gu, T. Wang and C. Wang, *J. Colloid Interface Sci.*, 2023, **636**, 255–266.

84 Z. Yuan, J. Cao, S. Valerii, H. Xu, L. Wang and W. Han, *Chem. Eng. J.*, 2022, **430**, 132755.

85 S.-J. Liu, S.-D. Han, Z. Chang and X.-H. Bu, *New J. Chem.*, 2016, **40**, 2680–2686.

86 Z. Yuan, J. Cao, D. Li, W. Wei, L. Wang and W. Han, *Appl. Surf. Sci.*, 2022, **597**, 153598.

87 Z. Yuan, L. Wang, D. Li, J. Cao and W. Han, *ACS Nano*, 2021, **15**, 7439–7450.

88 S. Shen, X. Xia, Y. Zhong, S. Deng, D. Xie, B. Liu, Y. Zhang, G. Pan, X. Wang and J. Tu, *Adv. Mater.*, 2019, **31**, 1900009.

89 O. Mashtalir, M. R. Lukatskaya, M.-Q. Zhao, M. W. Barsoum and Y. Gogotsi, *Adv. Mater.*, 2015, **27**, 3501–3506.

90 J. Xiao, B. Wu, L. Bai, X. Ma, H. Lu, J. Yao, C. Zhang and H. Gao, *Electrochim. Acta*, 2022, **402**, 139566.

91 W. Kang, Y. Wang and J. Xu, *J. Mater. Chem. A*, 2017, **5**, 7667–7690.

92 Y. Xiao, S. H. Lee and Y.-K. Sun, *Adv. Energy Mater.*, 2017, **7**, 1601329.

93 J. Cao, J. Li, D. Li, Z. Yuan, Y. Zhang, V. Shulga, Z. Sun and W. Han, *Nano-Micro Lett.*, 2021, **13**, 113.

94 L. Lu, G. Guan, J. Wang, W. Meng, S. Li, Y. Zhang and F. Guo, *Chem. Eng. J.*, 2024, **480**, 147999.

95 G. Wang, Z. Yang, X. Nie, M. Wang and X. Liu, *Micromachines*, 2023, **14**(8), 1515.

96 Y.-J. Lei, Z.-C. Yan, W.-H. Lai, S.-L. Chou, Y.-X. Wang, H.-K. Liu and S.-X. Dou, *Electrochem. Energy Rev.*, 2020, **3**, 766–792.

97 M. Mahajan, K. Roy, S. Parmar, G. Singla, O. P. Pandey, K. Singh, R. Vaidhyanathan and S. Ogale, *Carbon*, 2020, **161**, 108–116.

98 Q. Wu, D. Yan, X. Li, C. Yu and T. Yao, *Chem. Eng. J.*, 2020, **393**, 123596.

99 K. Subramanyan, S. Chen, N. Li, T. Ma, Y. Liu, S. Chandrasekaran and V. Aravindan, *Electrochim. Acta*, 2023, **437**, 141505.

100 S. Kanade, M. Gautam, A. Ambalkar, Y. Sethi, M. O. Thotiyl, B. B. Kale and A. B. Gambhire, *ACS Appl. Energy Mater.*, 2022, **5**, 1972–1983.

101 Y. Li, J. M. Cao, L. Li, Z. Yuan, D. Li, J. Li, Y. Zhang, H. Xu, W. Han and L. Wang, *Chem. Eng. J.*, 2023, **456**, 141005.

102 W. Tang, W. Zhong, Y. Wu, Y. Qi, B. Guo, D. Liu, S.-J. Bao and M. Xu, *Chem. Eng. J.*, 2020, **395**, 124978.

103 X. Yue, J. Wang, A. M. Patil, X. An, Z. Xie, X. Hao, Z. Jiang, A. Abudula and G. Guan, *Chem. Eng. J.*, 2021, **417**, 128107.

104 R. Liu, L. Yang, W. Wang, E. Zhao, B. Wang, X. Zhang, H. Liu and C. Zeng, *J. Mater. Sci. Technol.*, 2023, **34**, 101300.

105 S. Nam, P. Thangasamy, S. Oh, M. Mahato, N. Koratkar and I.-K. Oh, *Nanoscale*, 2020, **12**, 20868–20874.

106 W. Zhang, J. Peng, W. Hua, Y. Liu, J. Wang, Y. Liang, W. Lai, Y. Jiang, Y. Huang, W. Zhang, H. Yang, Y. Yang, L. Li, Z. Liu, L. Wang and S.-L. Chou, *Adv. Energy Mater.*, 2021, **11**, 2100757.

107 G. Liu, T. Zhang, X. Li, J. Li, N. Wu, A. Cao, W. Yuan, K. Pan, D. Guo and X. Liu, *Inorg. Chem. Front.*, 2023, **10**, 1587–1602.

108 L. Chen, M. Wang, E. Li, X. Hu, S. Huang, Z. Yang, D. Zhou, H. Xie, J. Chen, Z. Ma, B. Guo, B. Yu and X. Li, *Inorg. Chem. Front.*, 2023, **10**, 4087–4101.

109 S.-Q. Wei, C.-D. Wang, P.-J. Zhang, K.-F. Zhu, S.-M. Chen and L. Song, *J. Inorg. Mater.*, 2019, **35**, 139–144.

110 Y. Dall'Agnese, P.-L. Taberna, Y. Gogotsi and P. Simon, *J. Phys. Chem. Lett.*, 2015, **6**, 2305–2309.